JGR Solid Earth

RESEARCH ARTICLE
10.1029/2024JB029058

Flow and Deformation in Earth's Deepest Mantle: Insights From Geodynamic Modeling and Comparisons With Seismic Observations

Mingming Li[1], Jonathan Wolf[2,3,4], Edward Garnero[1], and Maureen D. Long[2]

[1]School of Earth and Space Exploration, Arizona State University, Tempe, AZ, USA, [2]Department of Earth and Planetary Sciences, Yale University, New Haven, CT, USA, [3]Department of Earth and Planetary Science, University of California, Berkeley, CA, USA, [4]Miller Institute for Basic Research in Science, Berkeley, CA, USA

Abstract The dynamics of Earth's D″ layer at the base of the mantle plays an essential role in Earth's thermal and chemical evolution. Mantle convection in D″ is thought to result in seismic anisotropy; therefore, observations of anisotropy may be used to infer lowermost mantle flow. However, the connections between mantle flow and seismic anisotropy in D″ remain ambiguous. Here, we calculate the present-day mantle flow field in D″ using 3D global geodynamic models. We then compute strain, a measure of deformation, outside the two large-low velocity provinces (LLVPs) and compare the distribution of strain with previous observations of anisotropy. We find that, on a global scale, D″ materials are advected toward the LLVPs. The strains of D″ materials generally increase with time along their paths toward the LLVPs and toward deeper depths, but regions far from LLVPs may develop relative high strain as well. Materials in D″ outside the LLVPs mostly undergo lateral stretching, with the stretching direction often aligning with mantle flow direction, especially in fast flow regions. In most models, the depth-averaged strain in D″ is >0.5 outside the LLVPs, consistent with widespread observations of seismic anisotropy. Flow directions inferred from anisotropy observations often (but not always) align with predictions from geodynamic modeling calculations.

Plain Language Summary The Earth's deep mantle deforms and moves at a geological timescale. This movement is called mantle convection which controls plate tectonics. Of particular importance is the flow in the lowermost few hundred kilometers of the mantle, which is called the D″ layer. The dynamics of D″ plays an essential role in Earth's thermal and chemical evolution. Direct observation of D″ flow is not possible, but D″ flow causes deformation of minerals that can align in preferential directions, leading to variable seismic velocities along different directions. This feature is called seismic anisotropy. In this study, we use numerical simulations to investigate D″ flow and its connection to rock deformation and seismic anisotropy. We find that D″ materials are strongly deformed, consistent with observations of seismic anisotropy in this layer. The strength of rock deformation in D″ generally increases with depth and increases toward regions beneath the Central Pacific and Africa, where two continental-sized seismic anomalies exist. Flow directions inferred from anisotropy observations often align with our numerical simulations. This study thus improves our understanding on the dynamics of the D″ layer.

Key Points:

- Geodynamic models show that D″ materials are strongly deformed, consistent with observations of seismic anisotropy
- Strains of materials in D″ generally increase with time as they go toward the large-low velocity provinces and deeper depths
- Flow directions inferred from anisotropy observations often align with that from geodynamic calculations

Supporting Information:

Supporting Information may be found in the online version of this article.

Correspondence to:

M. Li,
Mingming.Li@asu.edu

Citation:

Li, M., Wolf, J., Garnero, E., & Long, M. D. (2024). Flow and deformation in Earth's deepest mantle: Insights from geodynamic modeling and comparisons with seismic observations. *Journal of Geophysical Research: Solid Earth*, *129*, e2024JB029058. https://doi.org/10.1029/2024JB029058

Received 6 MAR 2024
Accepted 21 NOV 2024

Author Contributions:

Conceptualization: Mingming Li, Jonathan Wolf, Edward Garnero, Maureen D. Long
Funding acquisition: Mingming Li, Edward Garnero, Maureen D. Long
Investigation: Mingming Li, Jonathan Wolf, Edward Garnero
Methodology: Mingming Li, Jonathan Wolf, Edward Garnero, Maureen D. Long
Project administration: Mingming Li
Software: Mingming Li
Validation: Mingming Li
Visualization: Mingming Li, Edward Garnero

1. Introduction

A grand challenge in solid Earth science is to understand the Earth's mantle flow field, which controls deep mantle structures, the generation and mechanism of plate tectonics, and the Earth's long-term thermal and chemical evolution. The lowermost mantle flow is of particular interest because it regulates the heat flux at the core-mantle boundary (CMB) (e.g., Li & McNamara, 2018; Li et al., 2018; Nakagawa & Tackley, 2008) which is critical for generating the magnetic field (e.g., Larson & Olson, 1991; Olson et al., 2014; Zhang & Zhong, 2011) and is essential for Earth's thermal evolution (e.g., Christensen, 1985; Korenaga, 2008). It dictates the formation of mantle plumes (Gonnermann et al., 2004; Heyn et al., 2020; Li, 2023a; Li & Zhong, 2017) that cause surface volcanism (Morgan, 1971). Furthermore, the lowermost mantle greatly influences the morphology and internal structure of seismic anomalies such as the large low velocity provinces (LLVPs) and ultra-low velocity zones (e.g., Li et al., 2017; McNamara et al., 2010; Pachhai et al., 2021; Yuan & Li, 2022b). It causes topography on the CMB (e.g., Deschamps et al., 2018; Lassak et al., 2010; Yoshida, 2008) and also affects the process of core-mantle reactions (e.g., Kanda & Stevenson, 2006; Ko et al., 2022; Manga & Jeanloz, 1996). Moreover, it

Writing – original draft: Mingming Li
Writing – review & editing: Mingming Li, Jonathan Wolf, Edward Garnero, Maureen D. Long

controls the advection, distribution, mixing, and accumulation of compositional reservoirs in the Earth's deep interior (e.g., Hansen et al., 2023; Li, 2021, 2023b; Li & McNamara, 2022; McNamara & Zhong, 2005; Tackley, 2011; Zhang et al., 2010) and thus plays an essential role in Earth's chemical evolution.

The large-scale structure of Earth's lowermost mantle is dominated by two LLVPs (e.g., Garnero et al., 2016; Grand, 2002; Li & Romanowicz, 1996; Ritsema et al., 2004). Surrounding the LLVPs are regions with generally higher-than-average seismic velocities, which are often interpreted as former, relatively cold, subducted slabs (e.g., Lithgow-Bertelloni & Richards, 1998). Geodynamic modeling results have shown that flow in the lowermost mantle, on a global scale, moves away from subduction zones toward the LLVPs (Dziewonski et al., 2010; Steinberger & Holme, 2008; Walker et al., 2011; Yoshida, 2008). This flow pattern can explain the preferential formation of mantle plumes at LLVP's edges (e.g., Torsvik et al., 2010, 2016), since the basal thermal boundary layer thickens in flow directions and becomes most unstable at LLVP's edges (Li & Zhong, 2017). However, understanding lowermost mantle flow at a scale smaller than a few hundred kilometers is more challenging because the regional density and viscosity variations are not yet well understood (e.g., Li, 2023a).

When deformation is accommodated in the dislocation creep regime, mantle flow causes the alignment of individual crystals in an aggregate, leading to a variation of seismic velocity with propagation and polarization direction. Therefore, observations of seismic anisotropy at the base of the mantle can offer crucial insights into the deep mantle flow field (e.g., Romanowicz & Wenk, 2017; Wolf, Li, Long, & Garnero, 2024). Global seismic tomography has shown that the bulk of the lower mantle is (almost) isotropic, while strong seismic anisotropy can be found in D″ (Auer et al., 2014; Chang et al., 2015; French & Romanowicz, 2014; Moulik & Ekstrom, 2014; Nowacki & Cottaar, 2021; Romanowicz & Wenk, 2017). These global results are supported by regional investigations, which identify seismic anisotropy in many regions of D″ (e.g., Asplet et al., 2020, 2023; Garnero & Lay, 1997; Long, 2009; Nowacki et al., 2010, 2011; Wolf & Long, 2022; Wolf et al., 2023). In some regions, strong seismic anisotropy is observed outside and near the edges of the LLVPs, with weaker or absent anisotropy within the LLVPs (Cottaar & Romanowicz, 2013; Reiss et al., 2019; To et al., 2005). Observations of anisotropy in the D″ layer are often interpreted as being caused by the strong deformation and thus crystal-preferred orientation (CPO) of anisotropic minerals such as post-Perovskite (pPv), Bridgmanite (Bdg), and/or ferropericlase (e.g., Cottaar et al., 2014; Merkel et al., 2002; McNamara et al., 2003; Merkel et al., 2007; Yamazaki & Karato, 2007; Wenk et al., 2011), or by shape-preferred orientation (SPO) (e.g., Dobson et al., 2019). However, inferring mantle flow direction from measurements of seismic anisotropy remains challenging, because the connections among flow, deformation, and anisotropy are not well understood.

In this study, we perform global geodynamic models to calculate the present-day mantle flow field and. We introduce passive tracers into the model domain to track deformation history in D″ outside the LLVPs. We aim to gain a better understanding of the mantle flow field in D″ and its connection to observations of seismic anisotropy.

2. Methods

2.1. Setup of Convection Models

We solve the following non-dimensional conservation equations of mass and momentum and calculate the instantaneous mantle flow under the Boussinesq approximation:

$$\nabla \cdot \vec{u} = 0, \tag{1}$$

$$-\nabla P + \nabla \cdot (\eta \dot{\epsilon}) + [\mathrm{Ra}(T - B_c C - B_{\mathrm{ppv}}\Gamma)]\,\hat{r} = 0, \tag{2}$$

where $\vec{u}$, P, η, $\dot{\epsilon}$, Ra, and T are, respectively, the velocity, dynamic pressure, viscosity, strain rate, Rayleigh number, and temperature. B_c and C are respectively the buoyancy number and the fraction of an intrinsically dense compositional component. B_{ppv} is the buoyancy number that represents the density increase due to the Bdg to pPv phase transition and the Γ is the phase function. $\hat{r}$ is a unit vector in the radial direction. Equations 1 and 2 are solved using the CitcomS code (Zhong et al., 2008). The model domain ranges from the CMB to Earth's surface and is divided into 12 equal-volume caps with each cap containing $128 \times 128 \times 80$ elements. This leads to a lateral resolution at the CMB of ~28 km. The radial resolution in the lowermost 300 km of the mantle is refined to 15 km. The CMB is free slip. The top surface is free slip in most cases except in Case 6, where the present-day plate

motion is applied. Both the CMB and the top surface are isothermal with non-dimensional temperatures of 1.0 and 0.0, respectively.

The Rayleigh number Ra is defined as:

$$\mathrm{Ra} = \frac{\rho g \alpha \Delta T R^3}{\kappa \eta_0}, \tag{3}$$

where ρ is density, g is gravitational acceleration, α is thermal expansivity, ΔT is the reference temperature (e.g., the non-adiabatic temperature difference between surface and the CMB), R is Earth's radius, κ is thermal diffusivity, and η_0 is reference viscosity.

The buoyancy numbers B_c and B_{ppv} are defined as:

$$B_c = \frac{\Delta \rho_c}{\rho \alpha \Delta T}, \tag{4}$$

$$B_{\mathrm{ppv}} = \frac{\Delta \rho_{\mathrm{ppv}}}{\rho \alpha \Delta T}, \tag{5}$$

where $\Delta \rho_c$ the intrinsic density anomaly with respect to the background mantle and $\Delta \rho_{\mathrm{ppv}}$ is the density increase due to the pPv phase transition.

The phase function for the pPv phase transition is defined as:

$$\Gamma(\pi) = 0.5 + 0.5 \tanh\left(\frac{\pi}{\delta}\right), \tag{6}$$

where δ is the width of the phase transition, and the excess pressure π is defined as:

$$\pi = d - d_{\mathrm{ppv}} - \gamma(T - T_{\mathrm{ppv}}), \tag{7}$$

where d is the depth, d_{ppv} and T_{ppv} are the reference depth and temperature for the pPv phase transition, respectively, and γ is the Clapeyron slope. The phase function Γ varies from 0.0 for purely Bdg phase to 1.0 for purely pPv phase.

The viscosity depends on temperature, depth, and the presence of pPv phase, expressed as:

$$\eta = \eta_r \exp\left[E(0.5 - T) + \Gamma \ln\left(\eta_{\mathrm{ppv}}\right)\right], \tag{8}$$

where E is the activation coefficient for the temperature-dependent viscosity, and η_{ppv} is the viscosity change due to the pPv phase transition. The variable η_r is a prefactor that controls the depth dependence of viscosity. It is 1.0 in the upper mantle and 70.0 in the lower mantle for most cases. The variables E, η_{ppv} and η_r are free parameters tested in this study.

We assume a linear relationship between the density anomaly caused by thermal expansion ($\Delta \rho_T$) and the anomaly of seismic shear-wave velocity (δV_s), given by:

$$\frac{\Delta \rho_T}{\rho} = C_{v_s - \rho} \frac{\delta V_s}{V_s}, \tag{9}$$

where $C_{v_s - \rho}$ is the conversion factor. The change of temperature is related to thermal density anomaly via thermal expansivity by:

$$\delta T = -\frac{\Delta \rho_T}{\rho \alpha}. \tag{10}$$

The non-dimensional form of the temperature anomaly is given by:

$$\delta T' = \frac{\delta T}{\Delta T}. \tag{11}$$

Finally, the non-dimensional temperature field in our models is calculated by:

$$T = T_{\text{ave}} + \delta T', \tag{12}$$

where the T_{ave} is the 1D laterally averaged profile of the non-dimensional temperature taken from present-day temperature field of a previous 3D global geodynamic model in (Li & Zhong, 2019) and is given in Figure S1a in Supporting Information S1. In many cases, the LLVPs are treated as compositionally distinct materials. For this condition, the buoyancy field also includes the effect of intrinsic density anomalies in LLVPs in most models. Table S1 in Supporting Information S1 summarizes physical parameters used in this study.

2.2. Strain Calculation

Mantle flow causes deformation and, under certain conditions, orientation of minerals which can develop seismic anisotropy. Specifically, CPO develops when deformation of anisotropic minerals is accommodated via dislocation creep, which is generally favored by lower temperatures, higher stresses, and larger grain sizes (e.g., Frost & Ashby, 1982; Yamazaki & Karato, 2007). In this work, we assume that the base of the mantle is deforming in the dislocation creep regime (e.g., Karato, 1998). This assumption is consistent with (a) geodynamic modeling studies (McNamara et al., 2003) showing concentration of deformation in D″, (b) mineral physics experiments showing the D″ minerals are anisotropic (e.g., Dobson et al., 2019; Wu et al., 2017; Yamazaki et al., 2006), as well as (c) the observations that seismic anisotropy in the deep mantle is constrained to the lowermost few hundred kilometers of the mantle (e.g., Auer et al., 2014; French & Romanowicz, 2014). The nature of seismic anisotropy caused by CPO is controlled by geometry and amount of deformation.

Passive tracers are introduced into the model domain and are advected by the instantaneous mantle flow field. The tracers track the strain along their paths. We use the method of McNamara et al. (2003) to calculate strain on tracers. More detailed descriptions of this method are also given in (Mckenzie, 1979; Spencer, 1980). The maximum stretch λ_{max} is calculated as the positive square root of the maximum eigenvalue of the left Cauchy-Green deformation tensor $\boldsymbol{G}$ which is defined as:

$$\boldsymbol{G} = \boldsymbol{F} \cdot \boldsymbol{F}^T, \tag{13}$$

where $\boldsymbol{F}$ is the deformation tensor and $\boldsymbol{F}^T$ is its transpose. According to this definition, an undeformed particle has $\lambda_{\text{max}} = 1.0$. However, the strain for an undeformed particle is traditionally defined as 0.0. Therefore, following (McNamara et al., 2003), we quantify strain using $\lambda_{\text{max}} - 1$. The deformation tensor $\boldsymbol{F}$ is initially a unit tensor. It changes along the trajectories of tracers and is determined by integrating the velocity gradient tensor $\boldsymbol{L}$ via:

$$\frac{\partial F_{ij}}{\partial t} = L_{ik} F_{kj}. \tag{14}$$

The trajectory of tracers is controlled by the initial location of tracers. In this study, we assume that tracers start to accumulate strain at the time when they first sink across the top of the D″ layer, which we define as 300 km above the CMB. We initially introduce tracers at the top of the D″ layer. We aim to obtain such an initial distribution of tracers that after they are advected to their final locations within D″, they evenly sample all regions in D″. We take the following steps to achieve this goal. First, we evenly distribute tracers at their final positions in the D″ layer. Then, these tracers are advected backward-in-time until they reach their initial locations at the top of D″. We denote the time duration that a tracer takes to travel from its final to initial location as t^*. After we obtain the initial location of all tracers, they are advected forward-in-time with a time of t^* to their final positions in D″. Each tracer takes a different path and thus has a different t^*. As a result, each tracer is introduced to the model domain at a time of t^* before the present-day. Strain of tracers is calculated during the forward-in-time process starting from the initial locations of tracers where they have zero strains (or unity λ_{max}).

3. Results

3.1. Flow and Deformation for the Reference Model

We first present the results for our reference model, Case 1. In this case, the density and temperature structures are converted from tomography model S40RTS (Ritsema et al., 2011) using a conversion factor $C_{v_s-\rho} = 0.4$ between thermal density anomaly and S-wave velocity anomaly (Equation 9). Similar to previous studies (e.g., Hager & Richards, 1989; Liu & Zhong, 2016), the density anomaly in the topmost 300 km of the mantle is removed because its relationship with V_s anomaly may not be well captured by a linear scaling law, due to the presence of strong compositional variations. The LLVPs have been suggested to be made of compositionally distinct material that is intrinsically denser than the surrounding mantle (e.g., Jones et al., 2020; Li & McNamara, 2022; McNamara & Zhong, 2005; Mulyukova et al., 2015; Yuan & Li, 2022a; Yuan et al., 2023). We define LLVP regions where the V_s is less than −0.26%. With this definition, 30% of the area at 2,800 km depth in S40RTS model is occupied by LLVPs. To account for the intrinsic density anomaly of LLVPs, we assign a buoyancy number of $B_c = 0.4$ in the lowermost 600 km of the LLVP regions. The Rayleigh number is $Ra = 2 \times 10^8$. The viscosity of Case 1 follows Equation 8. The non-dimensional activation energy is $E = 9.21$, equivalent to a dimensional activation energy of 191 kJ/mol. Due to numerical challenges, we use a relatively low activation energy compared to that constrained by experiments, which is in the range of ∼240–530 kJ/mol (e.g., Karato & Wu, 1993); we explore the effects of temperature-dependence of viscosity in another case. The depth-dependent viscosity prefactor η_r is 1.0 in the upper mantle and 70.0 in the lower mantle. Parameters related to the pPv phase transition are $B_{\mathrm{ppv}} = 0.13$, $\gamma = 0.1456$, $d_{\mathrm{ppv}} = 0.42386$, $T_{\mathrm{ppv}} = 0.5$, and $\eta_{\mathrm{ppv}} = 0.01$. The laterally averaged viscosity profile is shown in Figure S1b in Supporting Information S1.

Because temperature scales linearly with V_s, the LLVP regions with lower V_s are generally hotter than their surroundings (Figure 1a). However, the majority of regions within the LLVPs remain negatively buoyant (Figure 1b). This is because the LLVPs in this model are assumed to be made of materials that are intrinsically denser than the background mantle. The temperature field controls the Bdg-pPv phase transition. At 2,800 km depth, regions outside the LLVPs are dominated by pPv phase, whereas no pPv phase exists within the hot LLVPs (Figure 1c). The fraction of pPv phase, as represented by the phase function Γ, varies with depth. For example, compared to at a depth of 2,800 km, the fraction of pPv phase is smaller at 45 km above the CMB and at depths near the top of D″ (Figure S2 in Supporting Information S1).

Results from our reference model (Case 1) show that flow in D″ generally converges toward the LLVPs (Figure 2a). Downwelling flows with negative radial velocity mostly occur far from LLVPs (e.g., beneath the circum-Pacific and Indian Ocean), whereas upwelling flows mainly occur within and just outboard of the LLVPs (Figure 2b). Flow in the lowermost mantle outside LLVPs is mostly in lateral directions. For example, the magnitude of radial velocity is ∼10 times lower than the lateral velocity at 2,800 km depth outside the LLVPs (Figure 2). In this study, we focus on flow and deformation outside LLVPs because the nature of internal convection within LLVPs is controlled by small-scale structures within LLVPs that may not be well resolved in global tomography models.

We calculate the second invariant of the strain rate tensors. The strain rate within D″ varies with depth (Figure 3). It is the lowest near the top of D″, reaches maximum values at intermediate depths of D″, and then decreases with depth toward the CMB (Figure 3). Specifically, strain rate is lower than 10^{-15} s^{-1} in all areas at 270 km above the CMB (Figure 3a). At 225 km above the CMB, strain rate becomes slightly higher than 10^{-15} s^{-1} in a few individual regions (Figure 3b). At about 180–90 km above the CMB, most regions outside the LLVPs have a strain rate larger than 10^{-15} s^{-1} (Figures 3c–3e). Regions with the highest strain rates include those beneath the central America, northwest of the Pacific LLVP, northeast of the African LLVP, and beneath the southeast of the African LLVP (Figures 3c–3e). At depths of 45 km above the CMB, the distribution of strain rate remains similar, except that its magnitude is reduced in most regions (Figures 3f–3h), compared to that at intermediate D″ depths. Noticeably, the regions with a strain rate around 3 - 4 × 10^{-15} s^{-1} at southeast of the African LLVP at mid-depth of D″ becomes less than 10^{-15} s^{-1} after 45 km above the CMB (Figures 3f–3h).

Next, we study strain in D″ (again, defined as the lowermost 300 km of the mantle). The computational domain contains 20 spherical shells in D″, so each shell has a thickness of 15 km. Each shell is further divided into 196,608 elements that are nearly equal surface area. First, we place one tracer at the center of each element, which gives 196,608 tracers within each shell that are evenly distributed. Then, we advect these tracers backward-in-

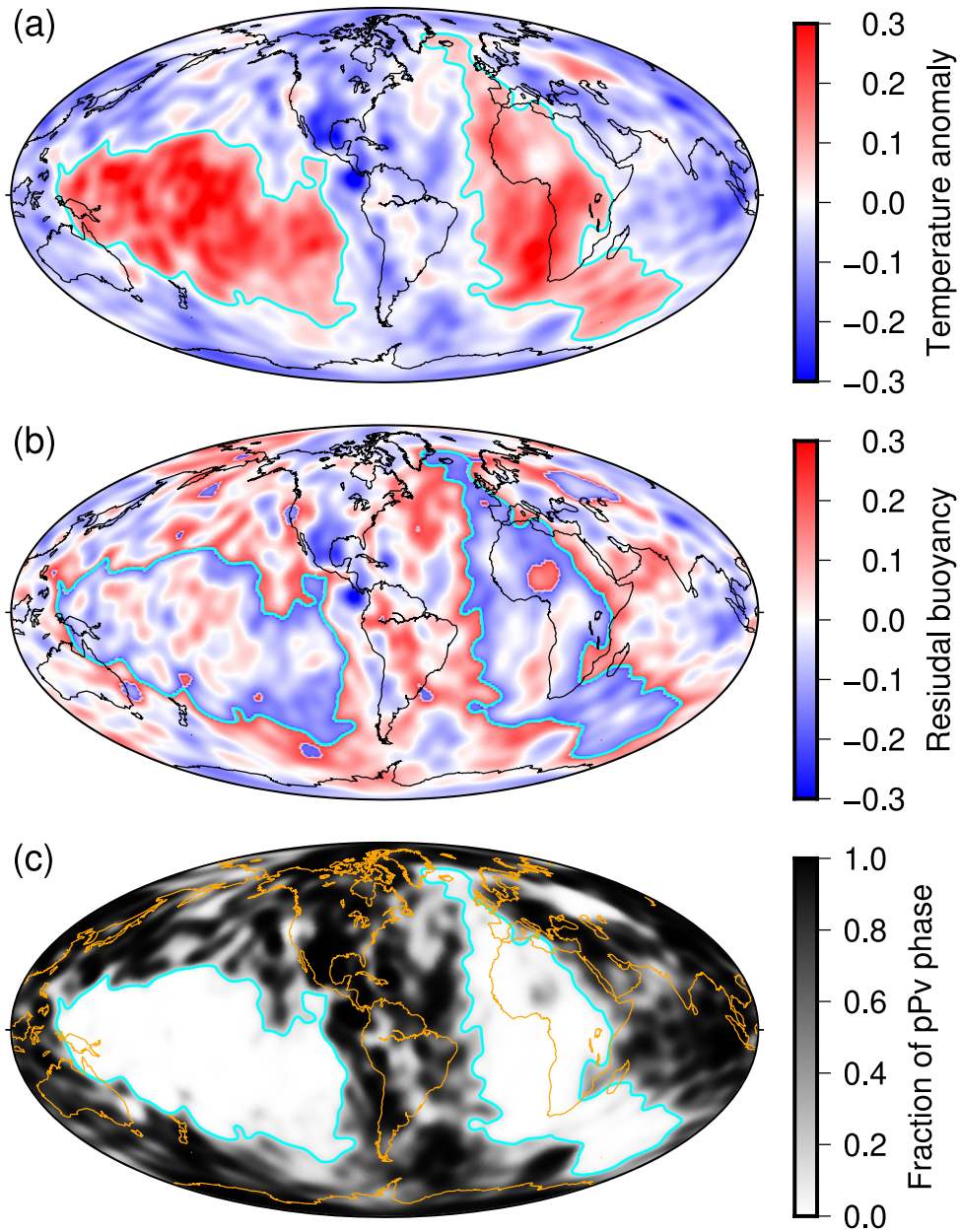

Figure 1. The distribution of (a) non-dimensional temperature anomaly after the horizontal average is removed, (b) residual buoyancy, and (c) the fraction of pPv phase as represented by the phase function Γ defined in Equation 6 (e.g., 1.0 indicates 100% pPv phase), at 2,800 km depth for Case 1. The cyan-contoured lines show large-low velocity province region boundaries at 2,800 km depth in the S40RTS tomography model.

time until they reach the top of D″. After that, these tracers are advected forward-in-time from the top of D″ to their final locations within D″ and we track the strain along tracer paths.

We first examine the strain of tracers at a depth of 97.5 km above the CMB, which is the central depth of the 7th shell when counting shells from the bottom. We find that most tracers, after they are advected backward to the top of D″, are located in regions with downwelling flows (Figure 2b) around the Pacific Ocean and the ancient Tethys Ocean (green colors in Figure 4a). Then, for tracers at the top of D″, we set their stretch (strain) to be unity (zero), advect them forward-in-time, and track their strains along their paths until present-day.

Again, we define the time it takes for a tracer to be advected from the top of D″ to their final locations (or 97.5 km above the CMB in this case) as t^*. We find that some tracers travel through the LLVPs, such as those near the

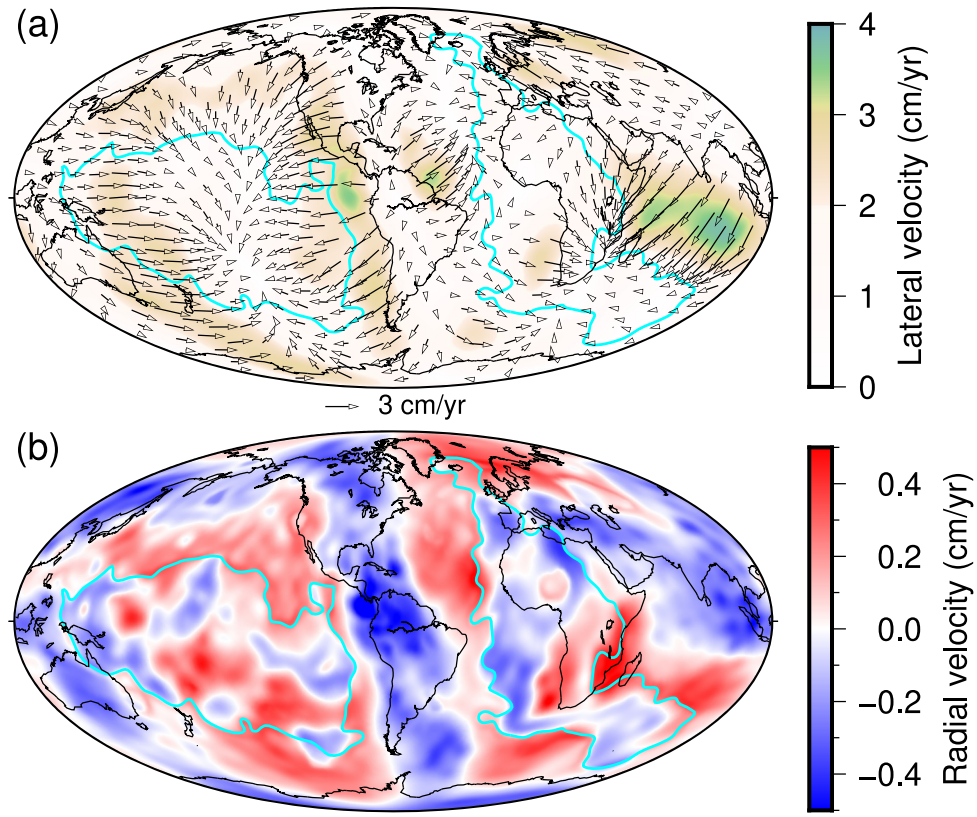

Figure 2. The distribution of (a) lateral flow velocity (arrows) and its magnitude (background) and (b) radial flow velocity at 90 km above core-mantle boundary for Case 1. The cyan contours show large-low velocity province regions at 2,800 km depth in the S40RTS tomography model.

northern portion of the African LLVP (Figure 4a). Because flow within LLVPs is uncertain (as we mentioned before), we do not show the deformation history of tracers that have traveled through LLVPs. The distribution of t^* is shown in Figure 4b. Generally, t^* increases toward the LLVPs. t^* in most regions outside the LLVPs is <100 Myr, with t^* < 50 Myr in downwelling centers. Most regions at the edges of LLVPs have t^* >100 Myr, except those that are close to downwelling centers such as the southeastern and western edges of Pacific LLVP and the northeastern edge of the African LLVP where the t^* can be <100 Myr. Except at the LLVP edges, some regions far from LLVPs also have t^* >100 Myr or even >150 Myr, including beneath the central U.S., south of the Pacific LLVP, and beneath northern Antarctica.

Figure 4c shows the strain distribution at 97.5 km above the CMB. Comparing Figures 4b and 4c, we find a clear spatial correlation between t^* and strain. For example, strains larger than 5.0 (e.g., white-brown colors in Figure 4c) often occur around the edges of the LLVPs where the t^* is typically >150 Myr. Some regions at the LLVP edges (such as the southeastern and western edges of Pacific LLVP and the northeastern edge of the African LLVP) show low strain, and these regions also have low t^* (Figure 4b). High strains are also found in regions far from LLVPs and these regions also show high t^*, although most regions far from LLVPs have both relatively low strain (e.g., <4.0) and relatively low t^* (e.g., <100 Myr). We calculate the average strain within each bin of t^*. We find that the average strain generally increases with t^* (Figure 4d), which again demonstrates that the strain is greatly controlled by t^*. The clear spatial correlation between t^* and strain indicates that the strain of tracer generally increases with time. This is not surprising because strain is a time-integration of the deformation history as shown in Equation 14.

Interestingly, regions with large t^* (e.g., >150 Myr, Figure 4b) and large strains (e.g., >5.0, Figure 4c) often exhibit linear shapes. Many of these linear-shaped regions such as around the Pacific LLVP or outside the two LLVPs, extend in directions that are parallel or sub-parallel to the surrounding flows. However, some of these regions such as along the western edges of the African LLVP are sub-perpendicular to the surrounding flows

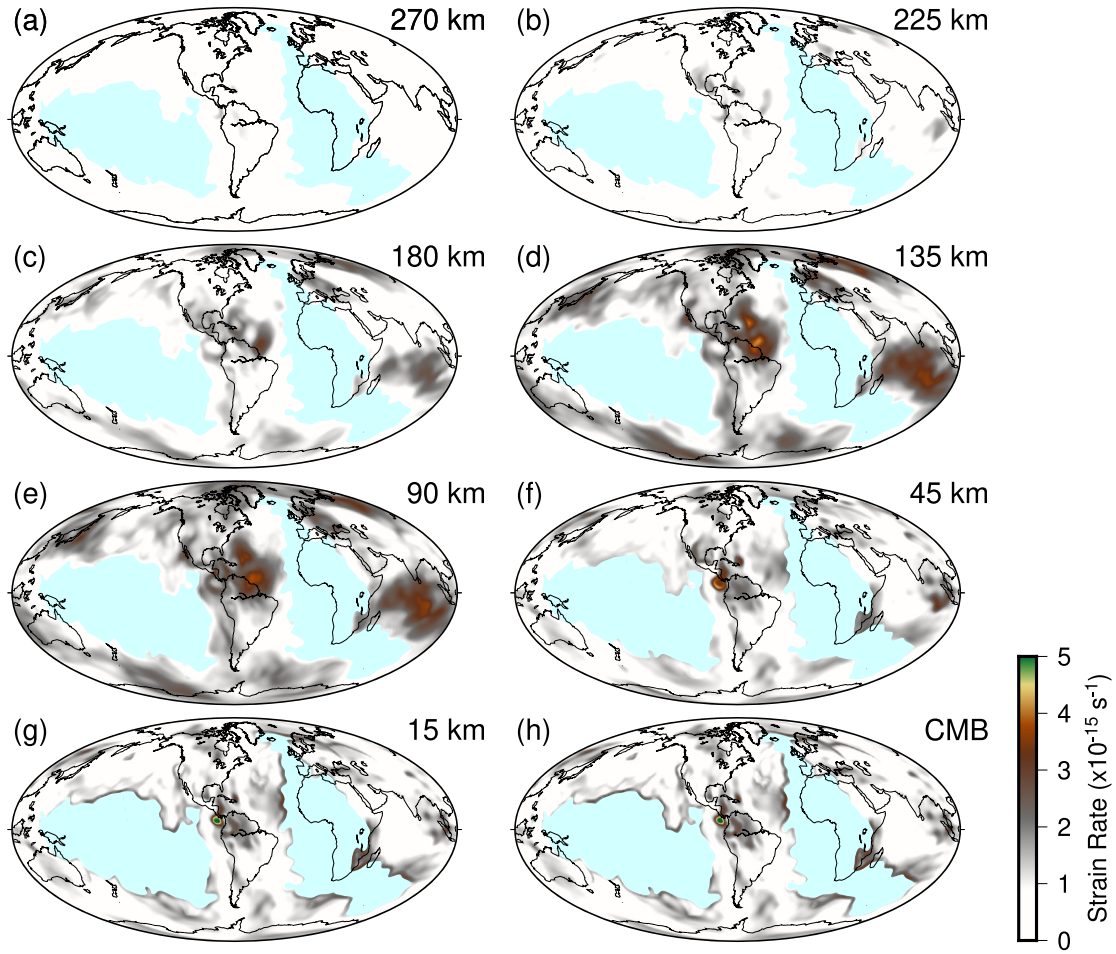

Figure 3. The second invariant of the strain rate tensor at depths of 270 km (a), 180 km (b), 135 km (c), 90 km (d), 45 km (e), and 15 km (f) above the core-mantle boundary (CMB) and at the CMB (h) for Case 1. The cyan patches show large-low velocity province regions at 2,800 km depth in the S40RTS tomography model.

(Figure 4b). Recall that tracers are advected, and their deformations accumulate, along streamlines. To better understand the spatial distribution of t^* and strain, we examine the trajectories and strain of tracers in two different regions, one beneath North America (Region 1) and the other beneath South America extending to the western edges of the African LLVP (Region 2).

Region 1 exhibits negative radial velocity ($v_{\text{rad}} < 0.0$ cm/yr) in most places, as indicated by the white contours in Figure 5a. Within this area, two sub-regions show significant negativity with $v_{\text{rad}} < -0.15$ cm/yr (blue contours in Figure 5a), separated by regions with less negative v_{rad}. We analyze the trajectories of four tracers in region 1. Tracers 1, 2 and 3 originate in areas with relatively slow downwelling speed and are advected westward along the flow. They spend all their time in areas with slow downwelling speed. Their final positions, although varying, remain aligned with the flow direction. Tracer 1 takes the longest path, tracer 3 the shortest, and tracer 2 an intermediate path. All three tracers sink consistently from 300 to 97.0 km above the CMB, except tracer 1, which goes upward during the last 10 Myr of its journey (Figure 5b) and ends in a region with positive v_{rad} (Figure 5a). Tracer 1 has the longest t^* of 144 Myr and the largest strain of 6.6, tracer 3 has the shortest t^* of 129 Myr and the smallest strain of 5.6, and tracer 2 has the intermediate t^* and strain (Figures 5b and 5c). We observe a slight decrease in strain for tracer 1 during its final trajectory (Figure 5c). In contrast, tracer 4 starts and spends more than 1/3 of its time in areas with significant negative v_{rad} (< -0.15 cm/yr) and reaches a final position similar to those of tracer 1 and 2 in just 80 Myr. Its present-day strain is 2.1–much smaller than tracer 1–3. These findings reinforce the notion that strain generally increases with time. They further imply that the linear-shaped high strain in Region 1 is likely due to the relatively weak downwelling flow along the paths of tracer 1–3, which prolonged their advection to their final position, leading to significant strain accumulation along their trajectories.

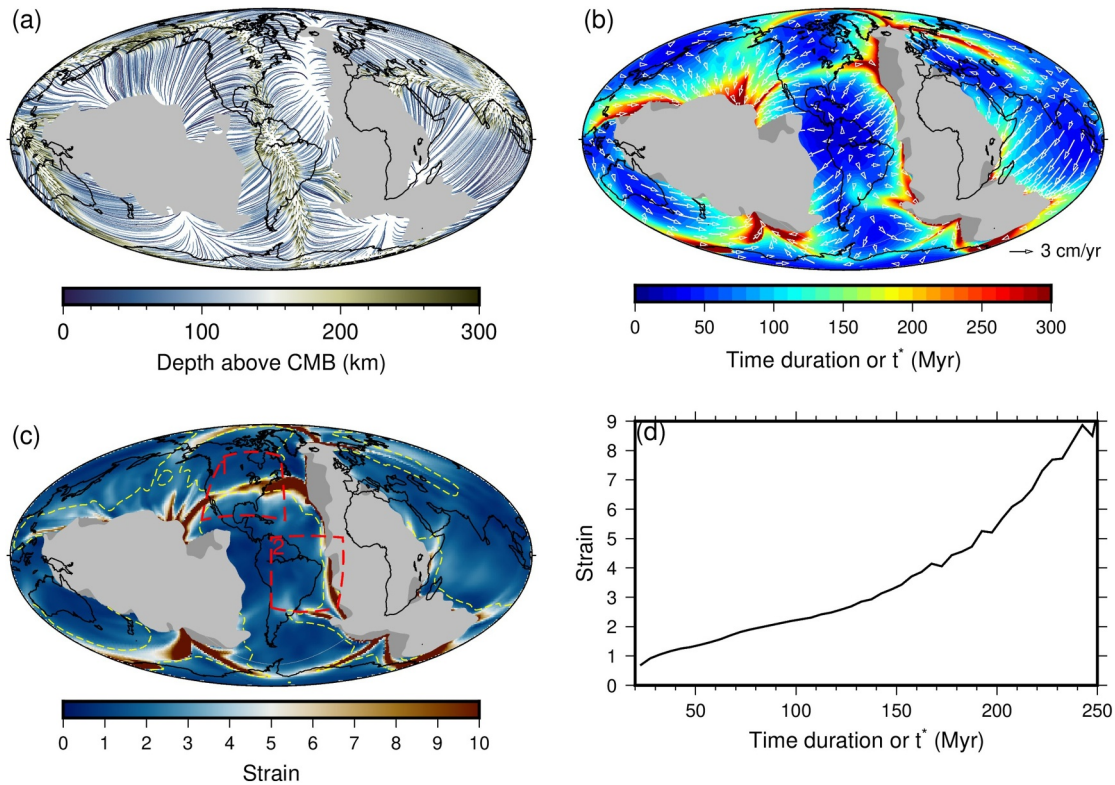

Figure 4. (a) The trajectories of tracers from the top of D″ to 97.5 km above the core-mantle boundary (CMB) for Case 1 with colors showing the heights of these tracers above the CMB. This panel shows the locations of the tracers over the time duration of these tracers. (b) The time duration t^* for these tracers to be advected from the top of D″ to 97.5 km above the CMB. White arrows show lateral flow velocity at this depth. (c) Strain at 97.5 km above the CMB. The dashed yellow lines are contours of $t^* = 120$ Myr. The zoomed-in view of the strains in the red boxes are shown in Figure 5. Lighter gray patches in panels (a–c) represent large-low velocity province (LLVP) regions at 2,800 km depth in the S40RTS tomography model, and darker gray patches are final locations of tracers that have traveled through LLVPs. (d) The average strain as a function of time duration t^*.

Region 2 exhibits a divergent flow field from a center near 5°S, 65°W, extending generally westward toward a linear, north-south high-strain zone (Figure 5d). We analyze the trajectories of four tracers in this region. All four tracers start at a close position with significant negative v_{rad} (< -0.15 cm/yr) and move westward with flow. They first traverse areas of negative v_{rad} before transitioning to areas of positive v_{rad} as they reach their final positions (Figure 5d). The distance-above-CMB profiles versus time for tracers 5, 6, and 7 nearly overlap (Figure 5e), indicating similar flow speed along their trajectories. However, although tracer 5 moves westward along its entire path, tracers 6 and 7 initially move westward before turning northward as they approach their final positions. Consequently, tracers 5, 6, and 7 end up aligned along a north-south line, perpendicular to the predominantly westward flow direction. These tracers share similar t^* of about 170 Myr and exhibit high strain at the present-day. The lower present-day strain of tracer 5 (at ∼5.9) than tracers 6 and 7 (at ∼8.2–8.8) may be due to the difference of strain rate along their trajectories. For comparison, tracer 8 starts near tracers 5–7 and reaches a final position near tracer 6. However, it is only advected for ∼117 Myr and accumulates a much smaller strain of ∼3.5 (Figure 5f), supporting the trend of strain increasing with time.

To summarize, tracers generally accumulate strain along flow directions. In regions where flow direction remains relatively stable, tracers that reach high strain values (>5.0) before their final positions continue accumulating strain, creating a high-strain track along streamlines parallel to the overall flow (Figures 5a–5c). However, when tracers initially exhibit low strain and only reach high strain after a 90-degree change in flow direction, high-strain regions will instead appear as linear zones perpendicular to the tracers' overall trajectories (Figures 5d–5f). Large strain gradients in some areas may result from materials requiring significantly different times to reach nearby final positions (e.g., tracer 4 and tracer 1 in Figure 5a and tracer 8 and tracer 6 in Figure 5d).

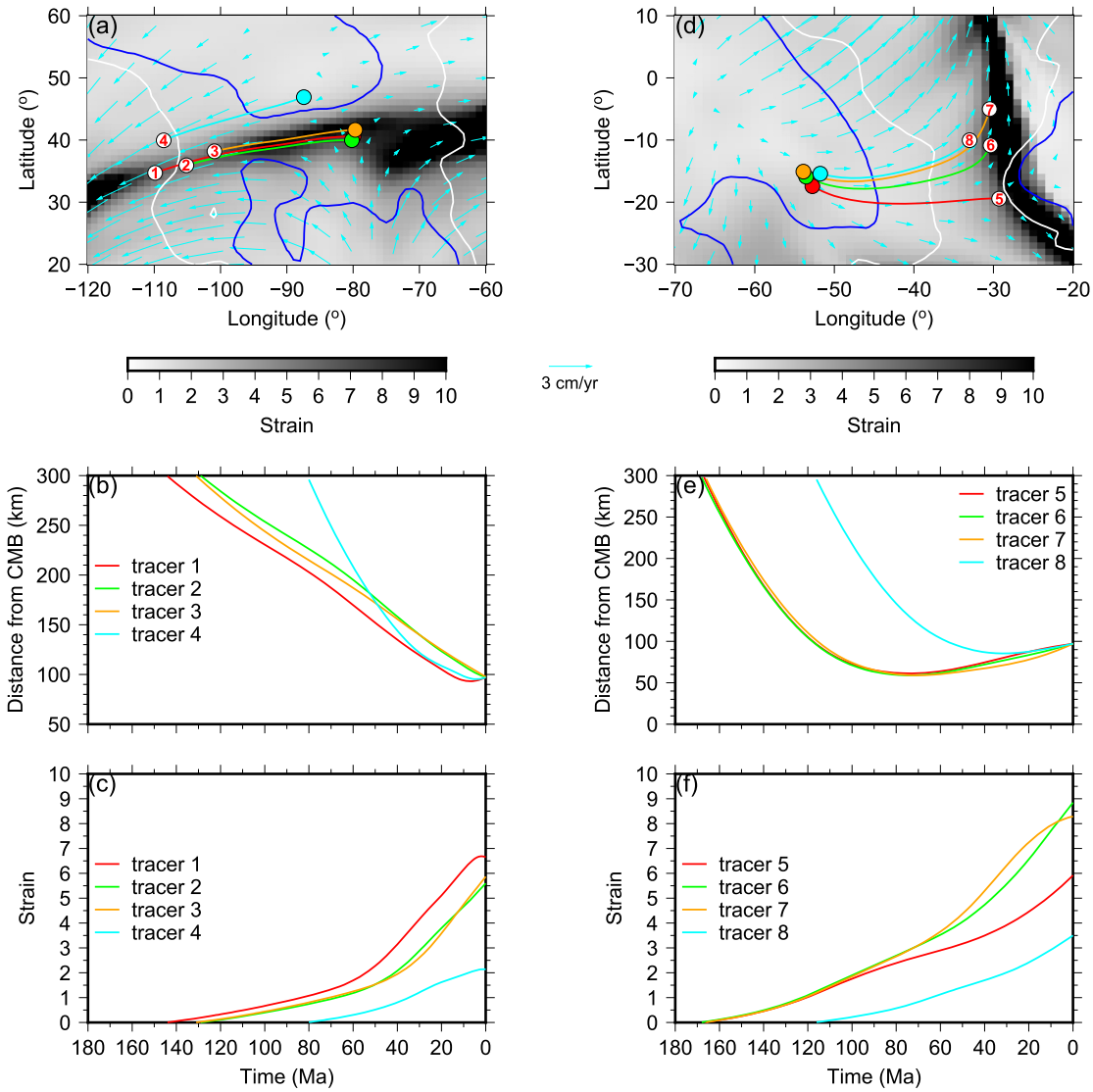

Figure 5. (a) Strain at 97.5 km above the core-mantle boundary (CMB) for Case 1 in Region 1 shown by the red box in Figure 4c at North America. The curves show the trajectories of tracers 1 (red), 2 (green), 3 (orange), and 4 (cyan). (b) The distance above the CMB for tracers 1–4 as a function of time. (c) The strain for tracers 1–4 as a function of time. (d) Strain at 97.5 km above the CMB for Case 1 in Region 2 shown by the red box in Figure 4c at South America. The curves show the trajectories of tracers 5 (red), 6 (green), 7 (orange), and 8 (cyan). The white circles and colored circles, respectively, show the final and initial locations of these tracers. (e) The distance above the CMB for tracers 5–8 as a function of time. (f) The strain for tracers 5–8 as a function of time. In panel (a) and panel (d), the white circles and colored circles, respectively, show the final and initial locations of these tracers. The numbers in white circles show tracer id. The cyan arrows are lateral flow velocities, and the white and blue curves are contours of radial velocity at 0.0 cm/yr and −0.15 cm/yr, respectively.

Returning to our global map of strain distribution, we find that about half of the tracers have strains larger than 1.8 at the present-day. Similarly, the magnitude of mantle flow velocity at present-day tracers' locations is larger than 1.5 cm/yr for about 50% of tracers. In order to gain intuition for the distribution of strain directions, we projected the maximum stretch direction in both lateral and radial directions. The directions of lateral strains are shown in Figure 6a together with mantle flow velocity. The ratio of radial strain to lateral strain is shown in Figure 6b. We find that this ratio is much less than 1.0 in most regions outside of LLVPs, except in a few regions at the LLVP's edges where it is higher than 1.0. This result indicates that materials outside of LLVPs are mostly laterally stretched except at the LLVP's margins where they are sometimes radially stretched. We quantify the angle between the direction of strains and the local flow velocity at each tracer's final location. We find that for tracers with strains larger than 1.8, approximately 75% of them exhibit an angle less than 30° (gray histograms in Figure 6c); this decreases slightly to ∼57% for tracers with strains smaller than 1.8 (red histograms in Figure 6c).

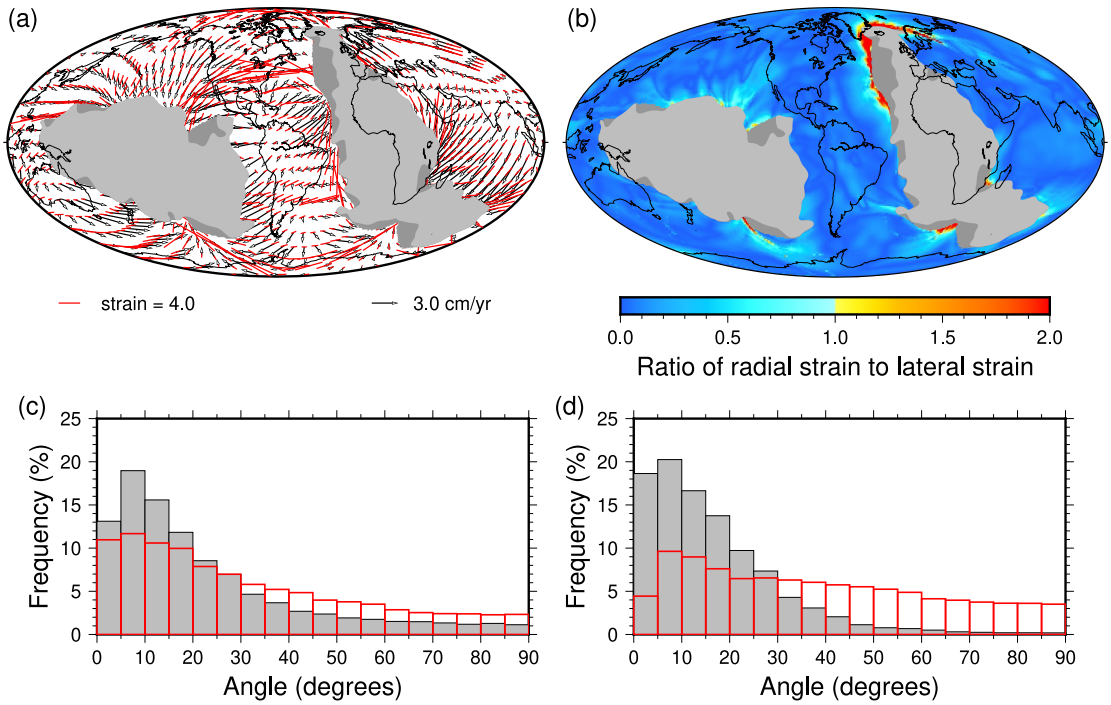

Figure 6. (a) The lateral flow velocities (black arrows) and the projections of the strains in the lateral directions (red bars) at 97.5 km above the core-mantle boundary for Case 1 outside the large-low velocity provinces (LLVPs). (b) The ratio of the magnitudes of radial to lateral strains, with blueish (reddish) colors indicate regions where lateral (radial) strains dominate. (c) The statistical distribution of the angles between the flow directions and the maximum stretch directions for strains larger than 1.8 (gray) and for strain smaller than 1.8 (red). (d) The statistical distribution of the angles between the flow directions and the maximum stretch directions for flow velocity larger than 1.5 cm/yr (gray) and for flow velocity smaller than 1.5 cm/yr (red). Lighter gray patches in panels (a, b) represent LLVP regions at 2,800 km depth in the tomography model S40RTS, and darker gray patches in panels (a, b) are final locations of tracers that have traveled through LLVPs.

For tracers with a present-day flow velocity larger than 1.5 cm/yr, approximately 86% of them exhibit angular differences between flow and strain direction less than 30° (gray histograms in Figure 6d). However, for tracers with a present-day flow velocity less than 1.5 cm/yr, only ~43% of them exhibit an angle less than 30°, and there is no preference of low angles for these tracers (red histograms in Figure 6d). Therefore, although the stretching directions of tracers generally agree with the mantle flow directions when tracers are strongly stretched in fast flow regions, this agreement does not generally hold for tracers that are not significantly stretched and/or are in slow flow regions at the present-day.

In Figures S3–S10 in Supporting Information S1, we present the tracer trajectories, t^* values, and strain values for Case 1 at depths of 277.5 km (Figure S3 in Supporting Information S1), 232.5 km (Figure S4 in Supporting Information S1), 187.5 km (Figure S5 in Supporting Information S1), 142.5 km (Figure S6 in Supporting Information S1), 97.5 km (Figure S7 in Supporting Information S1), 52.5 km (Figure S8 in Supporting Information S1), 22.5 km (Figure S9 in Supporting Information S1), and 7.5 km (Figure S10 in Supporting Information S1) above the CMB. All tracers are advected from top of D″ in downwelling centers to their final depths and locations. At 277.5 km above the CMB, the time duration t^* is less than 50 Myr in most regions outside the LLVPs, except regions near the LLVP's margins where t^* could be larger than 100 Myr. Regions with high strains (e.g., >5.0) only occur near the edges of LLVPs, whereas most regions far from LLVPs have strain <1.0 (Figure S3 in Supporting Information S1). As the depth of tracers increases toward the CMB, it takes more time for tracers to reach their final locations as represented by the increasing t^* with depth, and strain generally becomes larger. At all depths, regions with higher strain typically show larger t^*.

Motivated by the fact that shear wave splitting measurements typically represent a path-integrated measure of anisotropy throughout the D'' layer, we calculate the depth-averaged strain, $\bar{\epsilon}$, for the 20 shells within D″. $\bar{\epsilon}$ shows a similar distribution to the strain at 97.5 km above the CMB (Figure 7a). Specifically, $\bar{\epsilon}$ is >1.0 in ~98% of the region outside of LLVPs (gray curve Figure 7b). About 25% of the region outside the LLVPs has $\bar{\epsilon} > 4.5$ (gray curve in Figure 7b); these high-strain regions often have a linear shape, extending from outside the LLVPs to the

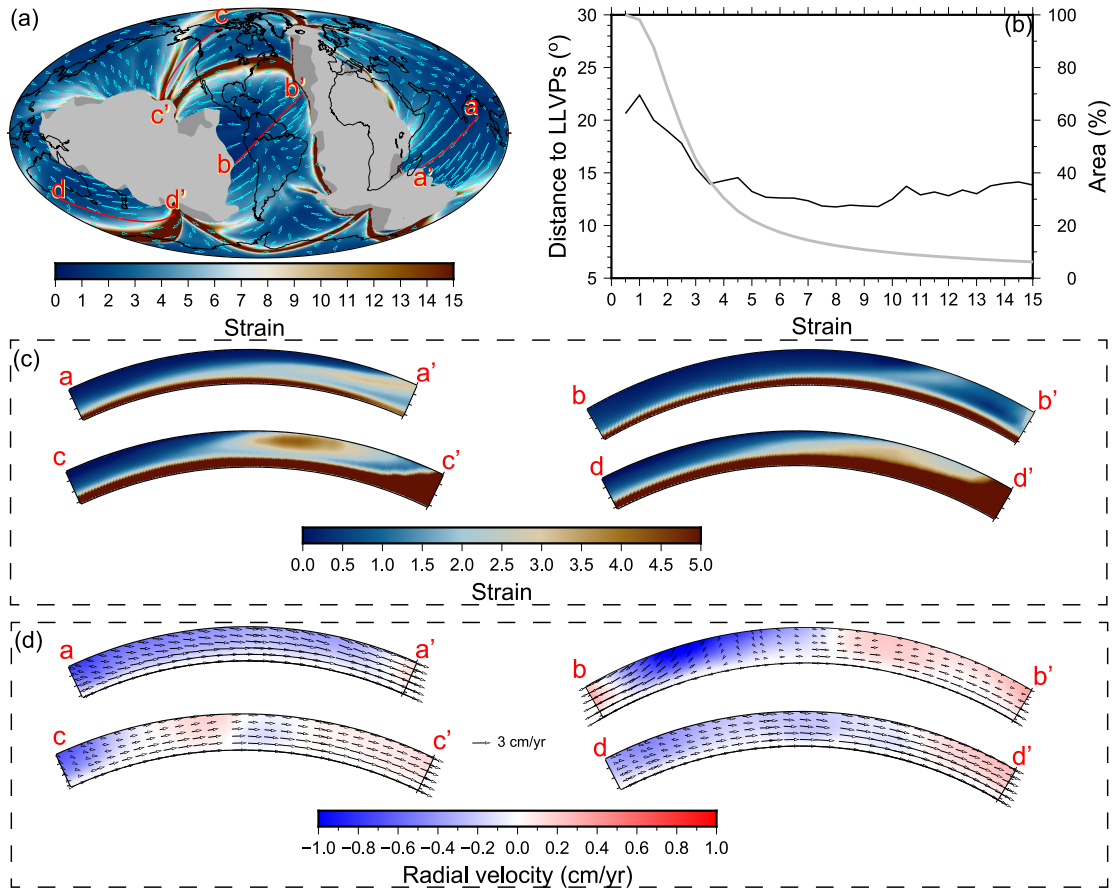

Figure 7. (a) The depth-averaged strain within D″ for Case 1. Cyan arrows show lateral flow velocity at 2,800 km depth. Lighter gray patches represent large-low velocity province (LLVP) regions at 2,800 km depth in the tomography model S40RTS, and darker gray patches are final locations of tracers that have traveled through LLVPs. (b) The average closest distance (black) to boundaries of LLVPs across regions with varying depth-averaged strains for the model without considering recrystallization and the areal percentage (gray) of these regions relative to the total map area excluding the LLVP regions and the regions affected by LLVPs. (c, d) Vertical cross-section of strain and flow velocity in the lowermost 300 km of the mantle in 4 locations as shown in panel (a).

margins of the LLVPs and along the edges of the African LLVP (Figure 7a). As shown by the black curve in Figure 7b, the average closest distance to the boundaries of LLVPs from regions with $\bar{\epsilon}$ between 0.5 and 1.5 is ~20–22°. This distance decreases to ~15° for higher stains and becomes relatively stable across regions with $\bar{\epsilon} > 3.5$.

Figures 7c and 7d show 4 vertical cross-sections of strain (Figure 7c) and velocity field (Figure 7d) along the lateral mantle flow directions as depicted in Figure 7a. Again, strain generally increases with depth and is highest at the base of the mantle (Figure 7c). The mantle flow is mostly lateral. The radial velocity is generally negative in regions away from LLVPs and positive near the edges of LLVPs. We find strain tends to increase in the lateral flow direction. However, the correlation between the vertical cross-sections of strain and flow velocity is not very clear, which may be because strains are computed from the time-integrated deformation along the trajectories of tracers, whereas the flow velocity only represents an instantaneous snapshot of the present-day. A better understanding of strain distribution requires analyzing the deformation history of materials such as shown in Figure 5.

In the real Earth, D″ may contain a mixture of the Bdg and pPv phases. Materials in D″ can be advected from a Bdg stability region to a pPv stability region, and vice versa. Materials experience recrystallization during phase changes, although the degree to which aggregates may retain fabrics inherited across a phase transition, known as topotaxy, remains imperfectly known (but may be important) (e.g., Chandler et al., 2021; Dobson et al., 2013; Walker et al., 2018). Recrystallization may also occur when materials are highly strained (e.g., Wenk et al., 1997). Importantly, recrystallization may cause the strength of preferred orientation, and thus the anisotropy of materials,

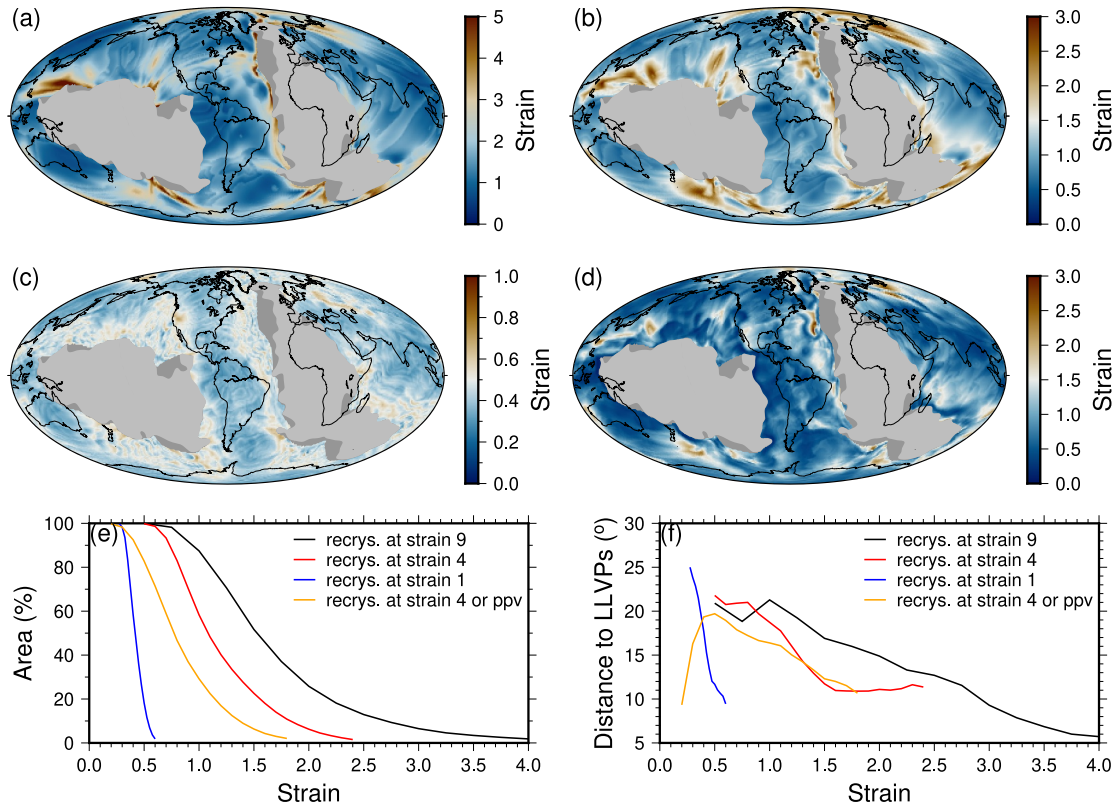

Figure 8. The distribution of the depth-averaged strain in the D″ layer for Case 1 under conditions: (a) when recrystallization occurs after reaching a strain of 9.0; (b) when recrystallization occurs after reaching a strain of 4.0; (c) when recrystallization occurs after reaching a strain of 1.0; and (d) when recrystallization occurs after reaching a stretch of 4.0 with additional recrystallization when materials are advected from the Bdg stability region (defined with $\Gamma<0.5$) to the pPv stability region (defined with $\Gamma > 0.5$) or vice versa. We approximate the effects of recrystallization on anisotropy strength by resetting the strain to zero when recrystallization occurs. Lighter gray patches represent large-low velocity province (LLVP) regions at 2,800 km depth in the tomography model S40RTS, and darker gray patches are final locations of tracers that have traveled through LLVPs. (e, f) The areal percentage of regions with respect to the global map regions excluding LLVP regions and regions affected by LLVPs (e) and the average closest distance to boundaries of LLVPs for cases under different conditions of recrystallization.

to decrease. However, the amount of anisotropy reduction due to recrystallization in lowermost mantle aggregates remains unclear. To approximate the process recrystallization and its effects on anisotropy, we assume a simplified, endmember scenario in which we consider the amount of strain as a proxy for anisotropy strength and parameterize the effects of recrystallization (including due to phase transitions) by resetting the strain to zero for each tracer after recrystallization.

We find that strain (i.e., our proxy for anisotropy strength) is reduced in D″ when the effect of recrystallization is considered (Figure S11 in Supporting Information S1). In addition, regions at deeper depths experience strain reduction in wider areas than those at shallower depths (Figure S11 in Supporting Information S1). This is because strain increases with depth and thus reaches the critical value for recrystallization more easily at deeper depths. The depth-averaged strain is also significantly reduced (Figures 8a–8d), and it is often much lower than the maximum strain set for recrystallization, as strain generally decreases with depth, and the strain at shallower depths is typically well below the maximum in most regions. If no recrystallization is considered, >98% of the area outside the LLVPs has $\overline{\epsilon} > 1.0$. However, if we set the critical value of strain for recrystallization at values of 9.0, 4.0, and 1.0, we find that more than 98% of the area outside the LLVPs has $\overline{\epsilon}$ larger than 0.75, 060, and 0.30, respectively (Figure 8e). When the maximum strain is set at 1.0, we observe a more dramatic spatial variation of strain values (Figure 8c) which is likely because of more frequent recrystallization. Interestingly, if recrystallization is considered only when a maximum is reached, the high strains observed far from LLVPs in the model without considering recrystallization become much smaller and no longer significant, and the high strains mostly occur around the edges of the LLVPs (Figures 8a–8c). Regions with higher strains are generally closer to the boundaries of LLVPs (Figure 8f). For the model with a critical maximum strain of 9.0, areas with the highest

Table 1
Parameters of Cases 1–7

Case	Nature of LLVPs	η_r in lower mantle	E	η_{ppv}	Plate velocity at surface	Tomography model
1	Thermochemical	70.0	9.21	0.01	No	S40RTS
2	**Purely thermal**	70.0	9.21	0.01	No	S40RTS
3	Thermochemical	**10.0**	9.21	0.01	No	S40RTS
4	Thermochemical	70.0	**0.00**	0.01	No	S40RTS
5	Thermochemical	70.0	9.21	**1.00**	No	S40RTS
6	Thermochemical	70.0	9.21	0.01	**Yes**	S40RTS
7	Thermochemical	70.0	9.21	0.01	No	**SEMUCB-WM1**

Note. Parameters different from Case 1 are bolded.

strain (the top 10%) reach a minimum distance of approximately 6–10° from the LLVP's boundaries. However, if we set the maximum strain to be 4.0 and also consider recrystallization due to phase transitions, we find that regions with the lowest strains tend to be closest to the LLVPs, although the distance still decreases with increasing strain for regions with strain >0.5 (orange curve in Figure 8f). The lowest strains (in this exercise, a proxy for anisotropy strength) at the LLVP's edges may be due to the pPv-to- Bdg phase transition in these relatively hot regions, causing recrystallization and strain reduction.

3.2. Investigating the Role of Model Parameter Variations

Deep mantle flow is controlled by the mantle density and viscosity structures, both of which involve significant uncertainties (e.g., Li, 2023a). Therefore, we carry out models with different mantle density and viscosity structures to study how the lowermost mantle flow and strain change. Table 1 lists parameters for cases 2–7. In Case 2, the LLVPs are treated as purely thermal structures; that is, with a buoyancy number of $B = 0.0$. In Case 3, we reduce the viscosity prefactor η_r in the lower mantle to 10; in other words, Case 3 has 7 times lower viscosity in the lower mantle than Case 1. In Case 4, we use $E = 0$, removing the temperature dependence of viscosity. In Case 5, we use $\eta_{ppv} = 1.0$, which effectively removes the change of viscosity due to the pPv phase transition. In Case 6, we apply present-day plate motions as the velocity boundary condition at the top surface. In Case 7, the thermal density anomaly is derived from a different tomography model, SEMUCB-WM1 (French & Romanowicz, 2014), and the LLVP regions are defined at regions where the V_s anomaly is less than - 0.41. Except for these changes, all other parameters for cases 2–7 are the same as that of Case 1.

Figure 9 shows the mantle velocities at 2,800 km depth for cases 2–7. We observe that the removal of the intrinsic density anomaly of the LLVPs in Case 2 does not induce significant changes to the lowermost mantle flow field (Figure 9a). By reducing the lower mantle viscosity by a factor of 7 in Case 3, the magnitude of the lateral flow velocities is increased by ∼4–5 times (Figure 9b; notice the different color-bar used in panel c). The removal of the temperature dependence of viscosity in Case 4 results in a minor reduction in velocity magnitudes and a smoother patten of the mantle flow velocities compared to Case 1 (Figure 9c). By removing the viscosity change in regions with pPv phase in Case 5, the magnitudes of mantle flow velocities are also reduced (Figure 9d). The use of present-day plate motion as the surface velocity boundary condition in Case 6 does not significantly alter the mantle flow field in the lowermost mantle (Figure 9e). By deriving the density field from a different tomography model of SEMUCB-WM1 in Case 7, the mantle flow field changes in localized regions, but the overall magnitudes of the flow velocities in the D″ layer remain similar (Figure 9f). Despite these variations of modeling results, the overarching convection pattern remains similar to Case 1. In each case, we observe mantle flow velocities moving from downwelling regions toward the two LLVPs, and regions around the edges of the LLVPs frequently exhibit positive upwelling flows (Figure 9).

Figure 10 shows the strain rate distribution at 90 km above CMB for cases 2–7. The spatial distribution of strain rate varies case by case. In general, for cases with increased (reduced) lowermost mantle flow velocity, they also have higher (lower) magnitude of strain rate. For example, the strain rate in Case 3 (Figure 10b), which uses reduced lower mantle viscosity that results in higher lowermost mantle flow velocities, is about 5 times higher

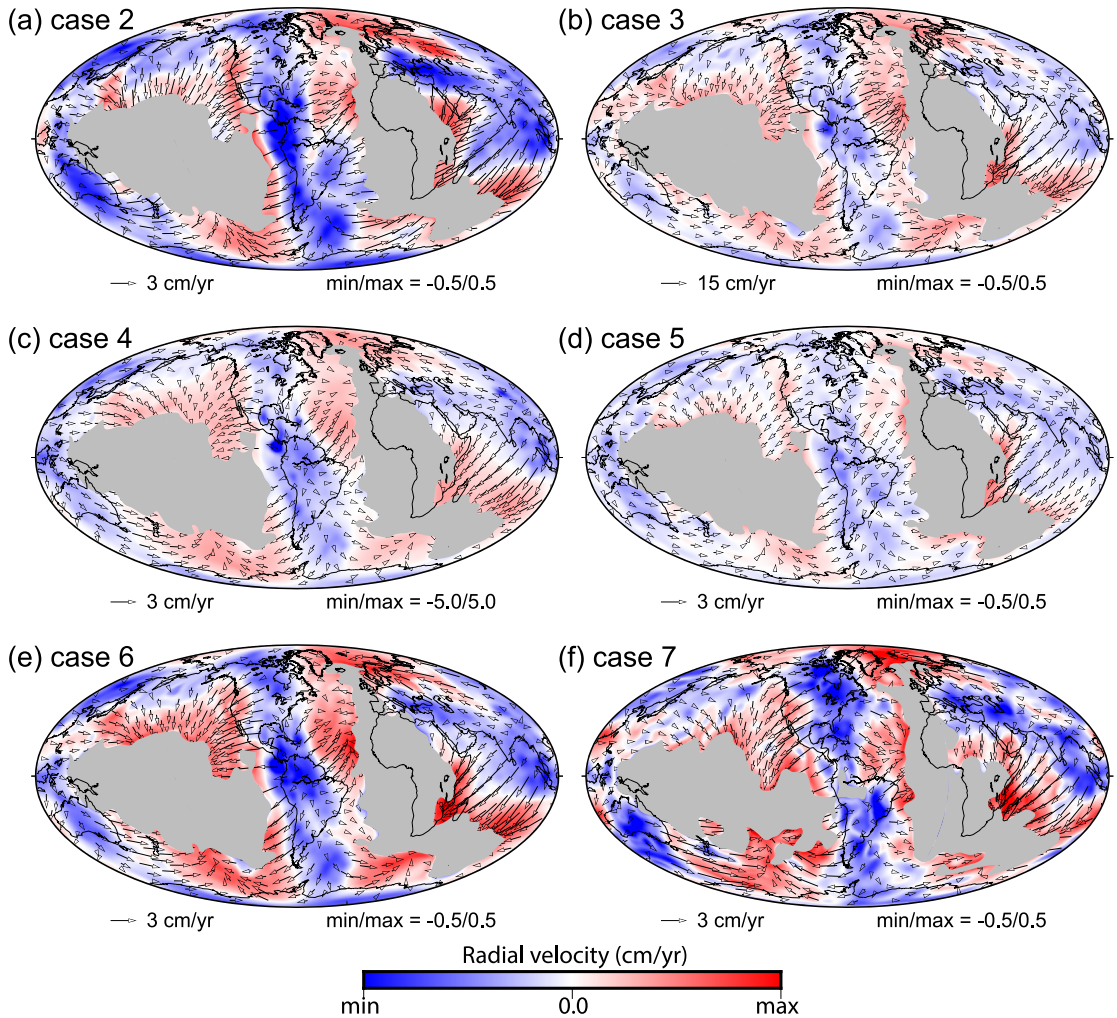

Figure 9. Mantle flow velocities for (a) Case 2, (b) Case 3, (c) Case 4, (d) Case 5, (e) Case 6, and (f) Case 7, at 2,800 km depth. The arrows show lateral flow velocity, and the background colors show radial flow velocity with reddish colors showing upward and blueish colors showing downward flow. The gray regions in panels (a–e) have V_s anomalies lower than −0.26% at 2,800 km depth in tomography model S40RTS and have V_s anomalies lower than −0.41% in tomography model SEMUCB-WM1 in panel (f), indicating the large-low velocity provinces.

than Case 1 (Figure 3e) although the two have similar spatial distribution of strain rate. However, the strain rate for Case 5 (Figure 10d) with reduced mantle flow velocity is ~5 times lower than Case 1 (Figure 3e).

Figure 11 shows the distribution of depth-averaged strain in D″ for cases 2–7 when recrystallization is considered after the strain reaches a value of 4.0. Note that although the maximum strain is set at 4.0, the strains in most regions, especially those at shallow depths of D″, are much lower than 4.0. As a result, the depth-averaged strain shown in Figure 11 is within a range of 0.0–3.0 in nearly all regions. We find that all cases show similar strain distribution to Case 1, showing high strains mostly around the edges of the LLVPs. If we do not consider the effects of recrystallization in these cases, the depth-averaged strain in D″ increases significantly, but the results remain generally similar to those for Case 1 (Figure S12 in Supporting Information S1). We also emphasize that although the strain rate for Case 3 (Figure 9b) is several times larger than Case 1, the strain distribution and magnitude are similar between the two cases. This may be because the mantle flow velocities in Case 3 are also faster than Case 1, such that tracers travel through the D″ layer more quickly. As a result, the accumulated amount of strain for each tracer, which is calculated by the product of the velocity gradient and the time, remains largely unchanged. We also perform a simulation that mimics Case 1 while doubling the lateral resolution and find that the strain is nearly the same (Figure S13 in Supporting Information S1).

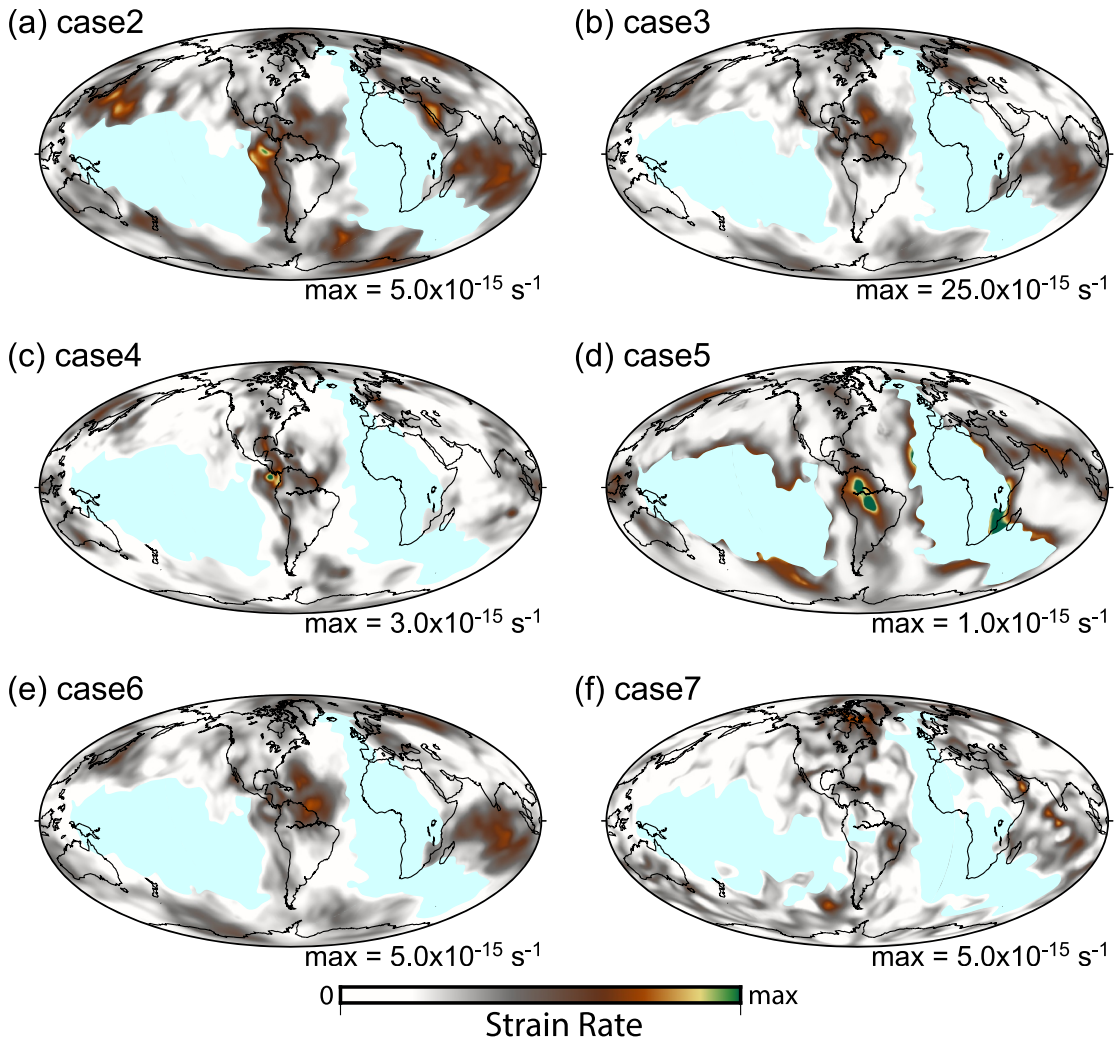

Figure 10. Strain rate at 90 km above the core-mantle boundary for Case 2 (a), Case 3 (b), Case 4 (c), Case 5 (d), Case 6 (e), and Case (7). The cyan regions in panels (a–e) have V_s anomalies lower than −0.26% at 2,800 km depth in tomography model S40RTS and have V_s anomalies lower than -0.41% in tomography model SEMUCB-WM1 in panel (f), indicating the large-low velocity provinces.

4. Discussion

4.1. Summary of Mantle Flow Field and Strain in D″ and Uncertainties

In this study, we calculate the present-day instantaneous mantle flow field in the mantle with a focus on regions outside the LLVPs in D″. We test different lower mantle viscosity and density structures. We find that the lowermost mantle flow velocities vary somewhat from model to model in localized regions; however, in all models examined in this study, materials in D″ move toward the two LLVPs (Figure 9), consistent with the D″ flow field reported in previous studies (e.g., Bull et al., 2010; Steinberger & Holme, 2008; Yoshida, 2008; Walker et al., 2011). In particular, the D″ mantle flow field outside the LLVPs is nearly the same when the LLVPs are treated as intrinsically dense materials or purely thermal structure (Figures 2a and 9a), suggesting that it is the downwelling flow (such as that associated with plate subduction) that controls mantle dynamics in these regions, not the LLVPs.

We find that strain generally increases along the trajectories of the tracers in D″. Generally speaking, the more time it takes for a tracer to be advected from the top of D″ to its final location within D″, the larger is strain at its final location (e.g., Figure 4d). Because mantle flow velocities generally move toward the LLVPs, strains also generally increase toward the edges of LLVPs (e.g., Figure 4c). However, some other regions, including beneath

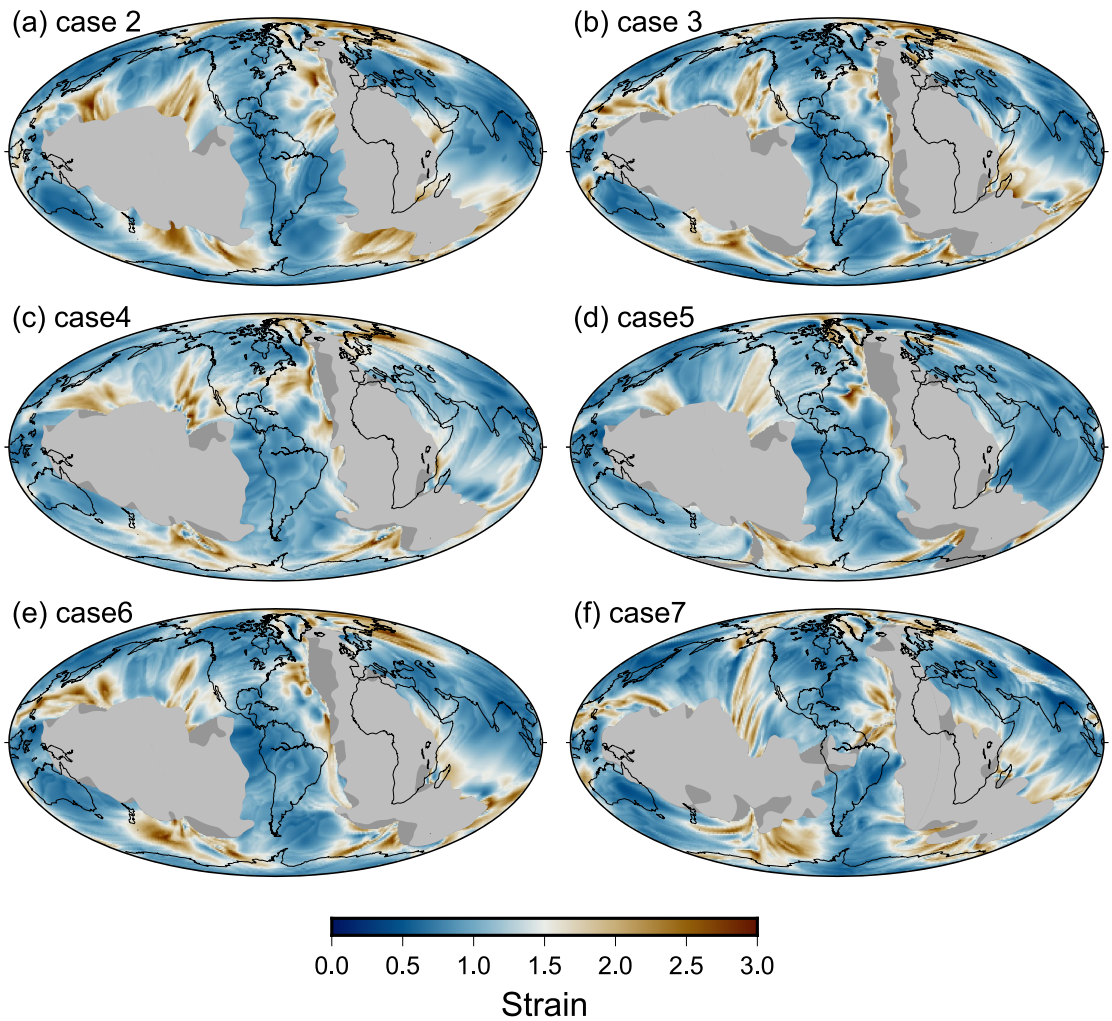

Figure 11. The distribution of the depth-averaged strain in the D″ layer when recrystallization occurs after reaching a stretch of 5.0 for (a) Case 2, (b) Case 3, (c) Case 4, (d) Case 5, (e) Case 6, and (f) Case 7. We approximate the effects of recrystallization on anisotropy strength by resetting the strain to zero when recrystallization occurs. Lighter gray patches represent large-low velocity province (LLVP) regions at 2,800 km depth in S40RTS model (a–e) and in the SEMUCB-WM1 model (f), and darker gray patches are final locations of tracers that have traveled through LLVPs. See Table 1 for model parameters for cases 1–7.

the central portions of North and South America, and near Antarctica, also exhibit relatively high strain (Figure 4c), consistent with the fact that it takes a relatively long time (e.g., high t^*) for tracers to reach these regions (Figure 4b). The large t^* in these regions may be related to their small and/or positive radial flow velocities (Figure 2b). Compared to the time that a tracer travels in D″, the instantaneous strain rate at the present-day plays a less important role in affecting the present-day strain. This is supported by the lack of clear spatial correlation between strain and strain rate distributions.

The magnitude of strain in D″ increases toward the CMB (Figures S3–S10 in Supporting Information S1). The depth-averaged strain in D″ exhibits a similar distribution as that at single depths in the mid-D″, showing high strains near LLVP edges and in a few regions far from the LLVPs (Figure 7a). The magnitude of anisotropy that results from CPO generated by strain can be greatly reduced if we consider the effects of recrystallization, which we approximate by resetting the strain to zero after it reaches a series of maximum threshold values of 9.0, 4.0 and 1.0 (Figures 8a–8c). In such cases, high strains still preferentially occur at the edges of LLVPs, but the high strains far from LLVPs, which are observed in the model without considering recrystallization, become much smaller and no longer significant. However, the strain at the LLVP edges can be significantly reduced as well (Figure 8d) if we consider recrystallization associated with the pPv to Bdg phase changes in these regions due to increased temperature.

We also find that materials in D″ outside the LLVPs are mainly stretched in the lateral direction, except near regions at the edges of LLVPs where they can be radially stretched (Figure 6b). The strains of some tracers can decrease with time along their paths, especially as the tracers go from downwelling to upwelling regions (e.g., tracer 1 in Figures 5a–5c). This may be because the increase of radial flow velocity increases stretching in radial directions but reduces stretching in the lateral directions. Furthermore, the maximum stretching directions often agree with mantle flow directions, especially for high strains in regions with fast mantle flow velocities (Figures 6a and 6c, 6d). However, this agreement often breaks down in regions with relatively slow flow velocities (Figure 6d). This may be because strains are computed from the time-integrated deformation along the trajectories of tracers, whereas the mantle flow velocities represent an instantaneous snapshot of the present-day mantle dynamics. The discrepancy between the two directions in some areas therefore indicates that the mantle flow field in these regions is not representative of the flow velocities throughout the trajectories of the tracers.

For simplicity, we use a constant scaling factor $C_{v_s-\rho}$ of 0.4 between V_s anomalies and density anomalies. Increasing or decreasing the value of $C_{v_s-\rho}$ will respectively increase or decrease the magnitude of density anomaly and thus the magnitude of mantle flow velocity, but the flow direction would remain the same. The comparison of modeling results between Case 3 and Case 1 suggests that the strain may also be insignificantly affected (Figures 7a and 11b). In reality, $C_{v_s-\rho}$ can vary with pressure, temperature, and composition (e.g., Steinberger & Calderwood, 2006). Steinberger and Holme (2008) considered these complexities and derived density anomalies from seismic velocities using mineral physical models. They showed that D″ flow generally moves toward the LLVP regions on a global scale, which is consistent with our models. This feature of D″ flow has been reported by other studies as well (Walker et al., 2011; Yoshida, 2008).

4.2. Comparison Between Geodynamic Modeling Results and Seismic Anisotropy Observations

Observations of seismic anisotropy can be used to infer flow present-day directions (e.g., Ford et al., 2015; Nowacki et al., 2010; Wolf & Long, 2023), although these inferences rely on (incomplete) knowledge of the relationships between strain and anisotropy for D″ minerals at realistic pressure and temperatures conditions (see Creasy et al., 2020; Wolf, Li, Long, & Garnero, 2024). In Figure 12, we show the direction of mantle flow in the D″ layer inferred from seismic anisotropy observations and that calculated from the geodynamic calculation in Case 1.

In theory, the deformation and flow inferred from our geodynamic modeling can be compared with the directions of mantle flow based on investigations of shear wave splitting in the lowermost mantle. However, such an exercise is challenging to perform in practice because inferring flow in the mantle from measurements of shear-wave splitting often relies on several assumptions, although substantial progress has been made recently (e.g., Romanowicz & Wenk, 2017; Wolf, Li, Long, & Garnero, 2024). For example, it is sometimes only possible to test whether the inferred seismic anisotropy is consistent with different geodynamic flow scenarios without uniquely constraining the flow geometry (e.g., Cottaar & Romanowicz, 2013; Reiss et al., 2019; Vanacore & Niu, 2011; Wolf et al., 2019), often due to the limitations intrinsic to the observational method (e.g., Reiss et al., 2019; Vanacore & Niu, 2011), limitations in ray coverage (e.g., Wolf et al., 2019) or both. In other cases, only a restricted range of flow directions is tested, for example, only horizontal flow (e.g., Wolf & Long, 2022; Wolf, Long, & Frost, 2024), arguing that other scenarios would be less geodynamically plausible. Some studies have related radial anisotropy to lowermost mantle flow without explicitly modeling flow (e.g., Kawai & Geller, 2010). This approach, however, also has its limitations because the commonly made assumption that larger velocities of horizontal than vertical particle motions indicate dominantly horizontal flow (and vice versa) is not always accurate (e.g., Yamazaki & Karato, 2007). To date, all studies known to us that have not made any restrictive assumptions about plausible flow scenarios have neglected full-wave effects, which have been shown to be important (e.g., Nowacki & Wookey, 2016; Wolf & Long, 2022). Many of these studies rely on the S-ScS differential splitting technique (Wookey et al., 2005), which can produce apparent D″ shear wave splitting in many cases, unless perfectly SH-polarized waves are used (Wolf & Long, 2024).

Due to these limitations, our comparison between flow directions predicted from our geodynamic modeling and those inferred from seismic anisotropy studies (Figure 12), distinguishes between studies whose interpretation of flow directions may be influenced by previous geodynamic modeling results (yellow circles in Figure 12) and studies that consider more degrees of freedom in their interpretations of flow from seismic anisotropy observations (yellow rectangles in Figure 12). As will be discussed later, however, there are still multiple assumptions

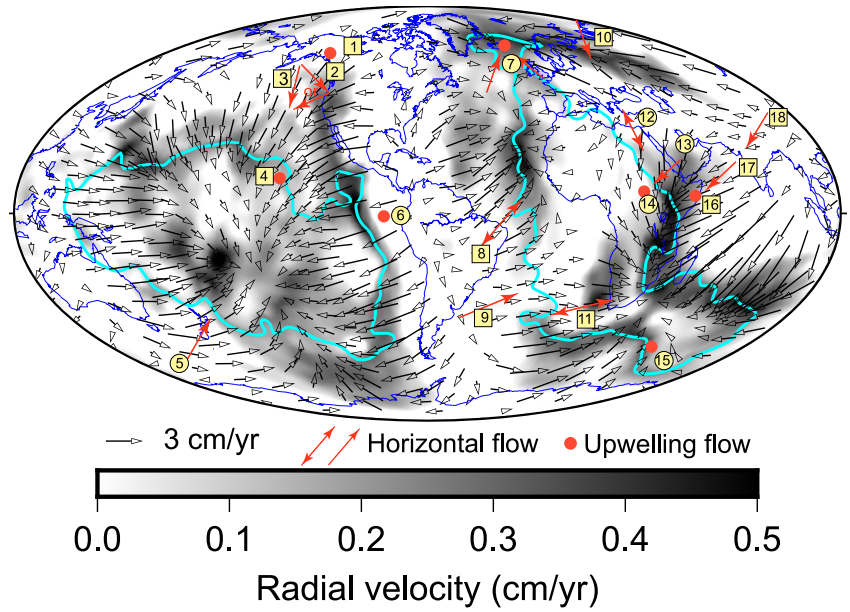

Figure 12. Comparison between mantle flow directions in the D″ layer based on previous seismic anisotropy studies (with red arrows showing lateral flow and red circles showing upwelling flows) and the flow velocities for Case 1 at 2,800 km depth (with black arrows showing lateral velocities and the background showing regions with positive radial velocities). Note that the red arrows indicate flow direction only at their midpoint; they do not represent magnitude. Numbers in yellow rectangle and circle boxes refer to the following citations: 1 = (Suzuki et al., 2021), 2 = (Asplet et al., 2023), 3 = (Wolf & Long, 2022), 4 = (Kawai & Geller, 2010; Wolf & Long, 2023), 5 = (Creasy et al., 2017), 6 = (Vanacore & Niu, 2011), 7 = (Wolf et al., 2019), 8 = (Pisconti et al., 2019), 9 = (Pisconti et al., 2023), 10 = (Creasy et al., 2021), 11 = (Pisconti et al., 2023), 12, 13, 14 = (Reiss et al., 2019), 15 = (Cottaar & Romanowicz, 2013), 16, 17 = (Ford et al., 2015; Reiss et al., 2019), 18 = (Wolf, Long, & Frost, 2024). Numbers in circles indicate studies in which the inference of mantle flow from observed anisotropy may be influenced by geodynamic modeling results. The cyan contours show large-low velocity province regions at 2,800 km depth in tomography model S40RTS.

that underlie these studies, which is an inevitable limitation when comparing geodynamic modeling results to seismic anisotropy.

Despite these challenges, we can see (e.g., through visual inspection) that the directions predicted from the two different approaches generally agree on a global scale, with both types of observations involving flow that is predominantly directed toward the two LLVPs (Figure 12). Specifically, the horizontal flow directions suggested by seismic studies in regions of #3, #8, #9, #11 and #17 generally agree with the geodynamic modeling results. The upwelling flows suggested by #4, #7, #15, and #16 are consistent with the positive radial velocity (darker shading in the figure) in the geodynamic model. Wolf et al. (2019) predicted converging and upwelling flows beneath Iceland in region #7, which also agrees with that from geodynamic calculation. Despite overall agreement, there are some significant disagreements between seismologically and geodynamically inferred flow directions, such as in regions #2, #10, and #18. A more quantitative and statistical comparison can be made when more and better estimates of flow directions based on seismic anisotropic observations become available.

Because it is technically deformation (strain) of anisotropic minerals in the D″ layer that causes seismic anisotropy, rather than flow itself, we next carry out a comparison between our predicted strain distributions and previous observations of lowermost mantle anisotropy. In Figure 13a, the red polygons show regions where D″ anisotropy has been reported in previous studies, as compiled by (Wolf et al., 2023), whereas the background map shows the depth-averaged strain in D″ after considering recrystallization at maximum strain of 4.0. Note that regions outside the red polygons generally represent portions of D″ that have not yet been surveyed by seismic studies; we do not intend to imply that they correspond to either isotropic or anisotropic D″ regions, as discussed in detail by (Wolf et al., 2023). Seismic anisotropy has been found in regions outside, at the edges, and within the LLVPs (Figure 13a). We compare these anisotropic locations to the distributions of the depth-averaged D″ strain for Case 1.

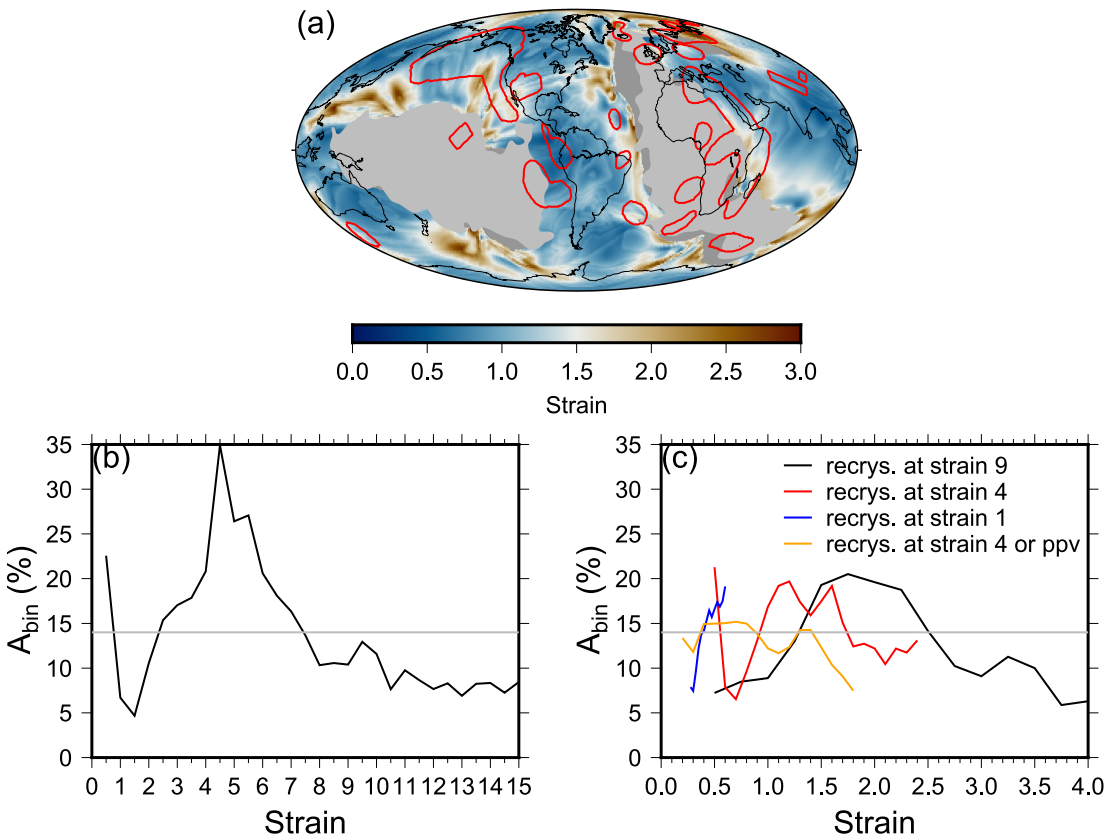

Figure 13. (a) Previous observations of seismic anisotropy (red polygons, Wolf et al., 2023) and the distribution of the depth-averaged strain in the D″ layer for Case 1 when recrystallization occurs after reaching a strain of 4.0. Strain is reset to be zero when recrystallization occurs. Lighter gray patches are regions where the V_s anomaly is less than −0.26% in the S40RTS tomography model at 2,800 km depth, showing the two large-low velocity provinces (LLVPs), and darker gray patches are the final locations of tracers that have traveled through LLVPs. (b, c) The percentage of the area exhibiting observed seismic anisotropy relative to the total area outside the LLVPs across a variety of strains. In panel (b), the strain is calculated without considering recrystallization effects. In panel (c), strain is calculated when recrystallization occurs at maximum strain of 9.0 (black), 4.0 (red), and 1.0 (blue), and when recrystallization occurs at maximum strain of 4.0 and also the tracer undergoes Bdg-pPv or pPv-Bdg phase transition (orange).

Mineral physics experiments have suggested that strains of 50% or less are sufficient to explain S-wave seismic anisotropy in D″ beneath the circum-Pacific rim (Wu et al., 2017). Here we find that, if recrystallization effects are ignored or included at a maximum strain of 4.0–9.0, all regions outside the LLVPs exhibit a strain greater than 0.5 (Figures 8a, 8b and 8d, 8e), which is consistent with widespread observations of seismic anisotropy in regions near the edges of the LLVPs (e.g., Deng et al., 2017; Lynner & Long, 2014; Reiss et al., 2019; Wang & Wen, 2007; Wolf & Long, 2023) or far away from the LLVPs (Figure 13) (e.g., Asplet et al., 2020; Garnero & Lay, 1997; Grund & Ritter, 2018; Long, 2009; Wookey et al., 2005; Wolf, Li, & Long, 2024). However, if recrystallization occurs at a maximum strain of 1.0, only ∼18% of the area outside the LLVPs exhibits strain >0.5 (Figures 8c and 8d). Therefore, recrystallization occurring at a maximum strain of 1.0 seems not to be realistic for Earth's D″; alternatively, our approximation of strain effectively resetting to zero after recrystallization is not realistic, which would imply that some frozen-in anisotropy remains after recrystallization.

One important question is whether regions with observed seismic anisotropy preferentially sample high strains, as predicted by our models. To address this question, we divide the range of strain outside the LLVPs into equal-sized strain bins. For each bin, we calculated the percentage of the area exhibiting observed seismic anisotropy relative to the total area outside the LLVPs and denote this percentage as A_{bin}. For reference, we also calculate the percentage of total area with observed seismic anisotropy outside the LLVPs to the total area outside the LLVPs, which is 14%. Therefore, for each strain bin, the result of $A_{bin} > 14\%$ indicates that the regions with observed seismic anisotropy preferentially sample strains within this strain. We find that when recrystallization is not considered, the anisotropic regions (as determined by seismic observations) preferentially correspond to

regions with strains of 0.5 and 2.5–7.0 (Figure 13b); that is, these regions have A_{bin} larger than 14%. When recrystallization is considered after maximum strain thresholds of 9.0, 4.0, and 1.0, the anisotropic regions preferentially correspond to regions with strains of 1.5–2.5 (black curve in Figure 13c), 0.5 and 1.0–1.7 (red curve in Figure 13c), and 0.4–0.6 (blue curve in Figure 13c), respectively. When recrystallization is considered, either after a maximum strain of 4.0 is reached or when minerals undergo a phase transition, the anisotropic regions preferentially correspond to regions with strains of 0.4–0.8 and 1.3–1.4 (orange curve in Figure 13c). We find that it is only for the case with recrystallization at maximum strain of 1.0 that the anisotropic regions slightly preferentially correspond to regions with the highest strains (blue curve in Figure 13c). However, it is worth emphasizing that seismic anisotropy may be present in many more regions than previously identified in regional studies, given the incomplete coverage of D″ in regional body wave studies to date (e.g., Wolf & Long, 2023).

4.3. Caveats and Uncertainties

In this section, we discuss the uncertainties in the calculations of mantle flow and strain in D″ and the considerable caveats involved in their comparison with flow and/or strain directions interpreted from seismic observations of anisotropy.

First, the geodynamically calculated D″ flow field and the resulting estimates of the strain field suffer from uncertainties in the present-day mantle density and viscosity structures, especially at relatively small scales (Li, 2023a). In particular, the temperature anomalies in our models are converted from seismic tomography models. Due to the limited spatial resolution of tomography models, our geodynamic models do not account for the influence of small thermal instabilities that remain unresolved in tomography models. As a result, the larger scale features of mantle flow velocity and strain in our models may be more robust than smaller-scale features.

Second, there are a number of uncertainties regarding our simplified treatment of recrystallization, which occurs when materials experience a phase transition or reach a critical amount of strain. We have implemented a simplified parameterization of recrystallization processes and find that the effective strain (our proxy for anisotropy strength) can be significantly reduced due to recrystallization. However, the magnitude of this reduction depends on the values of critical strain at which recrystallization starts, which are poorly known. Despite this uncertainty, we find that when recrystallization occurs at a maximum strain of 9.0 to 1.0, the highest strain tends to occur near the edges of the LLVPs, although the strain right at LLVP's edges can also be reduced when phase transition related recrystallization occurs at these regions.

Third, we assume that strain (as a proxy for anisotropy strength) effectively begins with value of zero at the top of D″. It is likely, however, that materials may have already been deformed before descending into D″, and it is possible that in the real Earth they may accumulate some fabric above the top of the D″ layer. As suggested by McNamara et al. (2003), the strength of anisotropy, as expressed via the proxy of (effective) strain, increases in regions where deformation is controlled by dislocation creep but decreases in regions of diffusion creep. Here, we assume that the deformation regime of materials sinking to D″ from above changes across the D″ boundary, diffusion creep in the bulk of the lower mantle to dislocation creep in the D″ layer. With this assumption, setting strain (as a proxy for anisotropy strength) to be zero at the top of D″ is reasonable to the first order. We note, as well, that mantle material passing through the Bdg-pPv phase transition at the top of D″ may experience a resetting of its texture, although some degree of crystallographic alignment may be inherited via topotaxy (e.g., Walker et al., 2018). We also note that the strain information carried by tracers that are advected to relatively deeper depths in D″ is strongly controlled by the trajectories of the tracers in D″, making the initial strain of these tracers less important. However, some studies have suggested that diffusion creep may play a significant role in deformation at the base of the mantle for pPv (Dobson et al., 2019) and Bdg (Reali et al., 2019), although this remains under debate (e.g., Karato, 1998; McNamara et al., 2002).

Fourth, our calculation of the deformation history is based on the instantaneous mantle flow field at the present day, because mantle flow in Earth's past history is not well constrained (e.g., Li, 2023a). In our calculations, each tracer takes a different amount of time to migrate from its initial location at the top of the D″ layer to its final location within D″. We find that for Case 1, this duration is typically less than 100 Myr in regions outside the LLVPs and is less than 50 Myr is downwelling regions (e.g., Figure 4b). It is longer at the edges of the LLVPs but still less than 200 Myr in most places (e.g., Figure 4b). The LLVPs have been suggested to be relatively stable in their locations at least during the past 200 Ma (e.g., Conrad et al., 2013; Torsvik et al., 2010). Thus, the first-order aspects of the lowermost mantle flow field over the past 200 Ma may be similar to the present day, at least at large

scales over the globe. Recently, Ward et al. (2024) compared the trajectories of tracers in D″ from models with constant flow and from models with time-dependent flow. They found that the path lengths of tracers in majority of D″ regions are similar between the two models (which indicates tracers in these regions take similar trajectories), but time-varying flow field can lead to significant deviation of tracer trajectories in some regions, especially for tracers that take long paths. This may be because the less we go back in time from present-day, the more closely the lowermost mantle flow field likely resembles that at the present-day (e.g., Li, 2023a). These findings and inference suggest that the calculated strain in our models may be more robust in regions beneath downwellings where tracers are advected for shorter durations and paths.

Fifth, there are some caveats when comparing geodynamic modeling results for the mantle flow field and strain distribution with seismic observations of anisotropy and their interpretation of flow directions. They include the following: (a) Seismic anisotropy has been observed within LLVPs interiors in some regions (e.g., Reiss et al., 2019; Wang & Wen, 2007), but we do not calculate strain in these regions. This is because the nature of small-scale internal convections within the LLVPs remains not well constrained, so predicting mantle flow within the LLVPs would be far less certain with our approach and thus requires future exploration. (b) For many regions with high strains in our models, no D″ anisotropy has been reported in previous studies. For many of these regions, this can be explained by a lack of seismic ray coverage, especially in the southern hemisphere (Wolf et al., 2023). In other cases where sampling is good, regions in which strain is high may be dominated by less anisotropic minerals, potentially Bdg (Romanowicz & Wenk, 2017). (c) In this study, we assume that seismic in D″ is caused by CPO, but seismic anisotropy could be caused by SPO of elastically distinct materials (such as partial melt) as well. (d) Seismic anisotropy contains information about the time-integrated deformation history of minerals and is affected by mantle flow history; therefore, the mantle flow directions interpreted from seismic anisotropy observations may not always agree with the present-day mantle flow direction (Figure 6). This may explain the disagreement of mantle flow directions in some regions of Figure 12. (e) Our models demonstrate that the strains in D″ often vary with depth, which agrees with the finding of (Ritsema et al., 1998), who showed that anisotropy may vary with depth. However, most D″ anisotropy observations reflect shear wave splitting due to anisotropy integrated along the D″ portion of the raypath. Depending on the specific seismic phases used in anisotropy measurements, seismic waves in D″ may sample anisotropy along a horizontal or oblique path, whereas the strains shown in Figures 8 and 11 are averaged along the radial (vertical) direction. (f) It remains unclear how large the strain of a lowermost mantle rock must be for it to develop anisotropy that is strong enough to be seismically detectable.

The comparison of flow directions between geodynamic models and flow directions inferred from global tomography models of radial seismic anisotropy is also challenging. On reason is that, the traditionally made assumption that $V_{SV} > V_{SH}$ indicates mainly vertical flow and vice versa does not always hold for seismic anisotropy caused by CPO (Yamazaki & Karato, 2007). A number of different minerals may contribute to lowermost mantle anisotropy (e.g., Creasy et al., 2020), including post-perovskite (e.g., Hirose et al., 2010; Miyagi et al., 2008; Yamazaki et al., 2006), bridgmanite (e.g., Miyagi & Wenk, 2016), and ferropericlase (e.g., Karki et al., 1999; Merkel et al., 2002), but the degree to which they contribute to seismic observations is not well constrained. For example, Yamazaki and Karato (2007) suggested that for a horizontal flow in D″, the Bdg phase will produce fast seismic velocity in radial direction (e.g., $V_{SV} > V_{SH}$), ferropericlase will produce fast seismic velocity in horizontal direction (e.g., $V_{SH} > V_{SV}$), and the fast direction of pPv phase depends on its elastic properties and dominant glide plane which remains under debate (Chandler et al., 2021; Cottaar et al., 2014; Merkel et al., 2007; Walker et al., 2011; Wenk et al., 2011; Wu et al., 2017). In other words, while radial anisotropy may give insights about the direction of flow in the upper mantle, simple blanket assumptions about the relationships between strain and anisotropy do not hold for D″ anisotropy due to these uncertainties.

If one was to take the position that most seismic anisotropy in D″ was caused by SPO, the assumption that $V_{SV} > V_{SH}$ indicates mainly vertical flow may hold better (Kendall & Silver, 1998). However, for global tomography models that show radial anisotropy, these models differ substantially (e.g., Auer et al., 2014; Chang et al., 2015; French & Romanowicz, 2014; Kustowski et al., 2008; Moulik & Ekstrom, 2014), except for the global-scale pattern that generally shows $V_{SV} > V_{SH}$ in and around LLVP regions and $V_{SH} > V_{SV}$ elsewhere. The large differences among the anisotropic tomography models may be partially caused by known tradeoffs between anisotropic structures and (sometimes shallower) isotropic structures for deep radial anisotropy inversions (e.g., Chang et al., 2015; Kustowski et al., 2008). Therefore, comparisons of flow with radial anisotropy patterns remain premature at this point. When comparing global radial anisotropy observations on a global scale, our geodynamic modeling results show strong upwelling flow within the LLVPs and at their edges and mainly lateral flow outside

LLVPs (e.g., Figures 2a and 2b), which is generally consistent with $V_{SV} > V_{SH}$ in and around LLVP regions and $V_{SH} > V_{SV}$ outside LLVPs under the assumption that seismic anisotropy is due to SPO. However, quantitative comparisons at smaller scales remain premature due to uncertainties in anisotropic tomography models.

Because of the caveats and uncertainties discussed above, it remains challenging to make specific and quantitative comparisons between geodynamic modeling of the D″ mantle flow field and flow inferred from seismic anisotropy studies. Reducing these uncertainties requires better constraints on the deep mantle viscosity and density structure, improvement in the spatial coverage in forward modeling studies of D″ anisotropy, and a more comprehensive understanding of the distribution of minerals in D″ as well as their elastic properties and deformation behavior. From an observational point of view, seismic characterization of regions with weak or absent seismic anisotropy, in addition to those that exhibit strong anisotropy, is essential. Future improvements in all these areas will lead to a greatly increased understanding of the patterns and drivers of flow at the base of Earth's mantle.

5. Conclusions

In this study, we explore the character of instantaneous mantle flow at the present day, with a focus on flow within the D″ layer. We show that for a range of geodynamic models with different density and viscosity structures, the flow typically moves away from regions beneath downwelling centers and toward the two LLVPs on a global scale, though the details of the D″ flow field vary across models in local regions. Relatively high strain rates are frequently found in regions surrounding the two LLVPs. Neither the mantle flow velocities nor the strain rates in the lowermost mantle outside the LLVPs are very sensitive to the density of the LLVPs, suggesting that the LLVPs themselves do not have a large influence on the mantle flow fields in D″ outside the LLVP's volumes.

We find that strain generally increases along the path of tracer in D″ toward the LLVPs. As a result, high-strain regions often occur near LLVP edges. However, it can take a long time for tracers to be advected to some regions far from LLVPs, and these tracers may develop high strains as well. Because it takes a long path and a long time for tracers to advected to deeper depths, strain is also highest at the CMB and decreases with the distance above the CMB. We approximate the effects of recrystallization by resetting the effective strain to be zero in our models when materials undergo phase transitions or reach a critical strain associated with recrystallization. When this recrystallization-induced strain reduction is considered, regions near LLVP margins often show higher strain than regions far from LLVPs. However, the post-perovskite to bridgmanite phase transition at LLVP edges may cause a significant reduction of anisotropy strength. When the recrystallization strain threshold is set at 4.0 or larger, almost all regions outside the LLVPs show effective strain >0.5, consistent with globally widespread observations of D″ anisotropy, but both relatively high and low strains are observed in regions with observations of seismic anisotropy. We also find that D″ materials outside LLVPs are mainly laterally stretched. The maximum stretch directions are often, though not always, similar to the mantle flow directions. These results suggest that some caution is warranted when interpreting seismically inferred anisotropy geometry at the base of the mantle as indicating present-day flow directions.

Flow directions have been inferred from seismic anisotropy observations in a few different locations in D″. It is encouraging to find that the flow direction in many of these locations agrees with that predicted from geodynamic modeling calculation. However, significant uncertainties remain in the predictions of strain and its connection to mantle flow field and the interpretations of seismic observations of anisotropy in terms of lowermost mantle flow; therefore, disagreement regarding the D″ flow direction from the two completely different approaches is to be expected. These uncertainties will be lessened as we improve our understanding of deep mantle density and viscosity structures, the distribution of mineral phases in the D″ layer, their elastic properties, and as we obtain more observations of lowermost mantle anisotropy.

Data Availability Statement

Supporting Information includes Figures S1–S13 and Table S1 in Supporting Information S1. The CitcomS code is open source and is available at CIG (Computational Infrastructure for Geodynamics) website https://geodynamics.org/resources/citcoms/supportingdocs. The authors' modified version of the CitcomS code, the input files, the data for initial conditions, and the data files used in each figure of this paper are available at (Li et al., 2024).

Acknowledgments
This work was funded by the National Science Foundation via Grants EAR-2054926 and EAR-2216564 to M. Li, Grant EAR-2026917 to M. D. Long, and Grant EAR-1855624 to E. Garnero. J. Wolf is supported by Yale University and the Miller Institute for Basic Research in Science, University of California Berkeley. We thank two anonymous reviewers and the editors for their constructive comments. Figures are plotted using the Generic Mapping Tools (www.soest.hawaii.edu/gmt/).

References

Asplet, J., Wookey, J., & Kendall, M. (2020). A potential post-perovskite province in D″ beneath the eastern Pacific: Evidence from new analysis of discrepant SKS–SKKS shear-wave splitting. *Geophysical Journal International*, *221*(3), 2075–2090. https://doi.org/10.1093/gji/ggaa114

Asplet, J., Wookey, J., & Kendall, M. (2023). Inversion of shear wave waveforms reveal deformation in the lowermost mantle. *Geophysical Journal International*, *232*(1), 97–114. https://doi.org/10.1093/gji/ggac328

Auer, L., Boschi, L., Becker, T. W., Nissen-Meyer, T., & Giardini, D. (2014). Savani: A variable resolution whole-mantle model of anisotropic shear velocity variations based on multiple data sets. *Journal of Geophysical Research*, *119*(4), 3006–3034. https://doi.org/10.1002/2013JB010773

Bull, A. L., McNamara, A. K., Becker, T. W., & Ritsema, J. (2010). Global scale models of the mantle flow field predicted by synthetic tomography models. *Physics of the Earth and Planetary Interiors*, *182*(3–4), 129–138. https://doi.org/10.1016/j.pepi.2010.03.004

Chandler, B. C., Chen, L.-W., Li, M., Romanowicz, B., & Wenk, H.-R. (2021). Seismic anisotropy, dominant slip systems and phase transitions in the lowermost mantle. *Geophysical Journal International*, *227*(3), 1665–1681. https://doi.org/10.1093/gji/ggab278

Chang, S. J., Ferreira, A. M. G., Ritsema, J., van Heijst, H. J., & Woodhouse, J. H. (2015). Joint inversion for global isotropic and radially anisotropic mantle structure including crustal thickness perturbations. *Journal of Geophysical Research*, *120*(6), 4278–4300. https://doi.org/10.1002/2014jb011824

Christensen, U. R. (1985). Thermal evolution models for the Earth. *Journal of Geophysical Research*, *90*(B4), 2995–3007. https://doi.org/10.1029/JB090iB04p02995

Conrad, C. P., Steinberger, B., & Torsvik, T. H. (2013). Stability of active mantle upwelling revealed by net characteristics of plate tectonics. *Nature*, *498*(7455), 479–482. https://doi.org/10.1038/Nature12203

Cottaar, S., Li, M., McNamara, A. K., Romanowicz, B., & Wenk, H.-R. (2014). Synthetic seismic anisotropy models within a slab impinging on the core–mantle boundary. *Geophysical Journal International*, *199*(1), 164–177. https://doi.org/10.1093/gji/ggu244

Cottaar, S., & Romanowicz, B. (2013). Observations of changing anisotropy across the southern margin of the African LLSVP. *Geophysical Journal International*, *195*(2), 1184–1195. https://doi.org/10.1093/gji/ggt285

Creasy, N., Long, M. D., & Ford, H. A. (2017). Deformation in the lowermost mantle beneath Australia from observations and models of seismic anisotropy. *Journal of Geophysical Research*, *122*(7), 5243–5267. https://doi.org/10.1002/2016jb013901

Creasy, N., Miyagi, L., & Long, M. D. (2020). A library of elastic tensors for lowermost mantle seismic anisotropy studies and comparison with seismic observations. *Geochemistry, Geophysics, Geosystems*, *21*(4), e2019GC008883. https://doi.org/10.1029/2019GC008883

Creasy, N., Pisconti, A., Long, M. D., & Thomas, C. (2021). Modeling of seismic anisotropy observations reveals plausible lowermost mantle flow directions beneath Siberia. *Geochemistry, Geophysics, Geosystems*, *22*(10), e2021GC009924. https://doi.org/10.1029/2021gc009924

Deng, J., Long, M. D., Creasy, N., Wagner, L., Beck, S., Zandt, G., et al. (2017). Lowermost mantle anisotropy near the eastern edge of the Pacific LLSVP: Constraints from SKS–SKKS splitting intensity measurements. *Geophysical Journal International*, *210*(2), 774–786. https://doi.org/10.1093/gji/ggx190

Deschamps, F., Rogister, Y., & Tackley, P. J. (2018). Constraints on core–mantle boundary topography from models of thermal and thermo-chemical convection. *Geophysical Journal International*, *212*(1), 164–188. https://doi.org/10.1093/gji/ggx402

Dobson, D. P., Lindsay-Scott, A., Hunt, S. A., Bailey, E., Wood, I. G., Brodholt, J. P., et al. (2019). Anisotropic diffusion creep in postperovskite provides a new model for deformation at the core−mantle boundary. *Proceedings of the National Academy of Sciences*, *116*(52), 26389–26393. https://doi.org/10.1073/pnas.1914826116

Dobson, D. P., Miyajima, N., Nestola, F., Alvaro, M., Casati, N., Liebske, C., et al. (2013). Strong inheritance of texture between perovskite and post-perovskite in the D″ layer. *Nature Geoscience*, *6*(7), 575–578. https://doi.org/10.1038/ngeo1844

Dziewonski, A. M., Lekic, V., & Romanowicz, B. A. (2010). Mantle Anchor Structure: An argument for bottom up tectonics. *Earth and Planetary Science Letters*, *299*(1–2), 69–79. https://doi.org/10.1016/j.epsl.2010.08.013

Ford, H. A., Long, M. D., He, X., & Lynner, C. (2015). Lowermost mantle flow at the eastern edge of the African large low shear velocity province. *Earth and Planetary Science Letters*, *420*(0), 12–22. https://doi.org/10.1016/j.epsl.2015.03.029

French, S. W., & Romanowicz, B. A. (2014). Whole-mantle radially anisotropic shear velocity structure from spectral-element waveform tomography. *Geophysical Journal International*, *199*(3), 1303–1327. https://doi.org/10.1093/gji/ggu334

Frost, H. J., & Ashby, M. F. (1982). *Deformation-mechanism maps: The plasticity and creep of metals and ceramics* (Vol. 175). Pergamon Press.

Garnero, E. J., & Lay, T. (1997). Lateral variations in lowermost mantle shear wave anisotropy beneath the north Pacific and Alaska. *Journal of Geophysical Research*, *102*(B4), 8121–8135. https://doi.org/10.1029/96JB03830

Garnero, E. J., McNamara, A. K., & Shim, S.-H. (2016). Continent-sized anomalous zones with low seismic velocity at the base of Earth's mantle. *Nature Geoscience*, *9*(7), 481–489. https://doi.org/10.1038/ngeo2733

Gonnermann, H. M., Jellinek, A. M., Richards, M. A., & Manga, M. (2004). Modulation of mantle plumes and heat flow at the core mantle boundary by plate-scale flow: Results from laboratory experiments. *Earth and Planetary Science Letters*, *226*(1–2), 53–67. https://doi.org/10.1016/j.epsl.2004.07.021

Grand, S. P. (2002). Mantle shear-wave tomography and the fate of subducted slabs. *Philosophical Transactions of the Royal Society of London Series a-Mathematical Physical and Engineering Sciences*, *360*(1800), 2475–2491. https://doi.org/10.1098/rsta.2002.1077

Grund, M., & Ritter, J. R. R. (2018). Widespread seismic anisotropy in Earth's lowermost mantle beneath the Atlantic and Siberia. *Geology*, *47*(2), 123–126. https://doi.org/10.1130/g45514.1

Hager, B. H., & Richards, M. A. (1989). Long-wavelength variations in Earth's geoid: Physical models and dynamical implications. *Philosophical Transactions of the Royal Society of London - Series A: Mathematical and Physical Sciences*, *328*(1599), 309–327. https://doi.org/10.1098/rsta.1989.0038

Hansen, S. E., Garnero, E. J., Li, M., Shim, S.-H., & Rost, S. (2023). Globally distributed subducted materials along the Earth's core-mantle boundary: Implications for ultralow velocity zones. *Science Advances*, *9*(14), eadd4838. https://doi.org/10.1126/sciadv.add4838

Heyn, B. H., Conrad, C. P., & Trønnes, R. G. (2020). How thermochemical Piles can (Periodically) generate plumes at their edges. *Journal of Geophysical Research*, *125*(6), e2019JB018726. https://doi.org/10.1029/2019JB018726

Hirose, K., Nagaya, Y., Merkel, S., & Ohishi, Y. (2010). Deformation of MnGeO3 post-perovskite at lower mantle pressure and temperature. *Geophysical Research Letters*, *37*(20), L20302. https://doi.org/10.1029/2010gl044977

Jones, T. D., Maguire, R. R., van Keken, P. E., Ritsema, J., & Koelemeijer, P. (2020). Subducted oceanic crust as the origin of seismically slow lower-mantle structures. *Progress in Earth and Planetary Science*, *7*(1), 17. https://doi.org/10.1186/s40645-020-00327-1

Kanda, R. V. S., & Stevenson, D. J. (2006). Suction mechanism for iron entrainment into the lower mantle. *Geophysical Research Letters*, *33*(2), L02310. https://doi.org/10.1029/2005gl025009

Karato, S., & Wu, P. (1993). Rheology of the upper mantle - A synthesis. *Science*, *260*(5109), 771–778. https://doi.org/10.1126/science.260.5109.771

Karato, S.-I. (1998). Some remarks on the origin of seismic anisotropy in the D″ layer. *Earth Planets and Space*, *50*(11), 1019–1028. https://doi.org/10.1186/BF03352196

Karki, B. B., Wentzcovitch, R. M., de Gironcoli, S., & Baroni, S. (1999). First-principles determination of elastic anisotropy and wave velocities of MgO at lower mantle conditions. *Science*, *286*(5445), 1705–1707. https://doi.org/10.1126/science.286.5445.1705

Kawai, K., & Geller, R. J. (2010). Waveform inversion for localized seismic structure and an application to D″ structure beneath the Pacific. *Journal of Geophysical Research*, *115*(B1), B01305. https://doi.org/10.1029/2009jb006503

Kendall, J.-M., & Silver, P. G. (1998). Investigating causes of D″ Anistropy. In *The core-mantle boundary region* (pp. 97–118). https://doi.org/10.1029/GD028p0097

Ko, B., Chariton, S., Prakapenka, V., Chen, B., Garnero, E. J., Li, M., & Shim, S.-H. (2022). Water-induced diamond formation at Earth's core-mantle boundary. *Geophysical Research Letters*, *49*(16), e2022GL098271. https://doi.org/10.1029/2022GL098271

Korenaga, J. (2008). Urey ratio and the structure and evolution of Earth's mantle. *Reviews of Geophysics*, *46*(2). https://doi.org/10.1029/2007rg000241

Kustowski, B., Ekström, G., & Dziewoński, A. M. (2008). Anisotropic shear-wave velocity structure of the Earth's mantle: A global model. *Journal of Geophysical Research*, *113*(B6), B06306. https://doi.org/10.1029/2007jb005169

Larson, R. L., & Olson, P. (1991). Mantle plumes control magnetic reversal frequency. *Earth and Planetary Science Letters*, *107*(3–4), 437–447. https://doi.org/10.1016/0012-821X(91)90091-U

Lassak, T. M., McNamara, A. K., Garnero, E. J., & Zhong, S. J. (2010). Core-mantle boundary topography as a possible constraint on lower mantle chemistry and dynamics. *Earth and Planetary Science Letters*, *289*(1–2), 232–241. https://doi.org/10.1016/j.epsl.2009.11.012

Li, M. (2021). The cycling of subducted oceanic crust in the Earth's deep mantle. In *Mantle convection and surface expressions* (pp. 303–328). https://doi.org/10.1002/9781119528609.ch12

Li, M. (2023a). The influence of uncertain mantle density and viscosity structures on the calculations of deep mantle flow and lateral motion of plumes. *Geophysical Journal International*, *233*(3), 1916–1937. https://doi.org/10.1093/gji/ggad040

Li, M. (2023b). Variable distribution of subducted oceanic crust beneath subduction regions of the lowermost mantle. *Physics of the Earth and Planetary Interiors*, *341*, 107063. https://doi.org/10.1016/j.pepi.2023.107063

Li, M., & McNamara, A. K. (2018). The influence of deep mantle compositional heterogeneity on Earth's thermal evolution. *Earth and Planetary Science Letters*, *500*, 86–96. https://doi.org/10.1016/j.epsl.2018.08.009

Li, M., & McNamara, A. K. (2022). Evolving morphology of crustal accumulations in Earth's lowermost mantle. *Earth and Planetary Science Letters*, *577*, 117265. https://doi.org/10.1016/j.epsl.2021.117265

Li, M., McNamara, A. K., Garnero, E. J., & Yu, S. (2017). Compositionally-distinct ultra-low velocity zones on Earth's core-mantle boundary. *Nature Communications*, *8*(1), 177. https://doi.org/10.1038/s41467-017-00219-x

Li, M., Wolf, J., Garnero, E. J., & Long, M. D. (2024). Flow and deformation in Earth's deepest mantle: Insights from geodynamic modeling and comparisons with seismic observations [Dataset]. *figshare*. https://doi.org/10.6084/m9.figshare.25330288.v3

Li, M., & Zhong, S. (2019). Lateral motion of mantle plumes in 3-D geodynamic models. *Geophysical Research Letters*, *46*(9), 4685–4693. https://doi.org/10.1029/2018gl081404

Li, M., & Zhong, S. J. (2017). The source location of mantle plumes from 3D spherical models of mantle convection. *Earth and Planetary Science Letters*, *478*, 47–57. https://doi.org/10.1016/j.epsl.2017.08.033

Li, M., Zhong, S. J., & Olson, P. (2018). Linking lowermost mantle structure, core-mantle boundary heat flux and mantle plume formation. *Physics of the Earth and Planetary Interiors*, *277*, 10–29. https://doi.org/10.1016/j.pepi.2018.01.010

Li, X. D., & Romanowicz, B. (1996). Global mantle shear velocity model developed using nonlinear asymptotic coupling theory. *Journal of Geophysical Research*, *101*(B10), 22245–22272. https://doi.org/10.1029/96JB01306

Lithgow-Bertelloni, C., & Richards, M. A. (1998). The dynamics of Cenozoic and Mesozoic plate motions. *Reviews of Geophysics*, *36*(1), 27–78. https://doi.org/10.1029/97rg02282

Liu, X., & Zhong, S. J. (2016). Constraining mantle viscosity structure for a thermochemical mantle using the geoid observation. *Geochemistry, Geophysics, Geosystems*, *17*(3), 895–913. https://doi.org/10.1002/2015gc006161

Long, M. D. (2009). Complex anisotropy in D″ beneath the eastern Pacific from SKS–SKKS splitting discrepancies. *Earth and Planetary Science Letters*, *283*(1), 181–189. https://doi.org/10.1016/j.epsl.2009.04.019

Lynner, C., & Long, M. D. (2014). Lowermost mantle anisotropy and deformation along the boundary of the African LLSVP. *Geophysical Research Letters*, *41*(10), 3447–3454. https://doi.org/10.1002/2014GL059875

Manga, M., & Jeanloz, R. (1996). Implications of a metal-bearing chemical boundary layer in D″ for mantle dynamics. *Geophysical Research Letters*, *23*(22), 3091–3094. https://doi.org/10.1029/96gl03021

Mckenzie, D. (1979). Finite deformation during fluid-flow. *Geophysical Journal of the Royal Astronomical Society*, *58*(3), 689–715. https://doi.org/10.1111/j.1365-246X.1979.tb04803.x

McNamara, A. K., Garnero, E. J., & Rost, S. (2010). Tracking deep mantle reservoirs with ultra-low velocity zones. *Earth and Planetary Science Letters*, *299*(1–2), 1–9. https://doi.org/10.1016/j.epsl.2010.07.042

McNamara, A. K., van Keken, P. E., & Karato, S.-I. (2002). Development of anisotropic structure in the Earth's lower mantle by solid-state convection. *Nature*, *416*(6878), 310–314. https://doi.org/10.1038/416310a

McNamara, A. K., van Keken, P. E., & Karato, S. I. (2003). Development of finite strain in the convecting lower mantle and its implications for seismic anisotropy. *Journal of Geophysical Research*, *108*(B5), 2230. https://doi.org/10.1029/2002jb001970

McNamara, A. K., & Zhong, S. (2005). Thermochemical structures beneath Africa and the Pacific Ocean. *Nature*, *437*(7062), 1136–1139. https://doi.org/10.1038/nature04066

Merkel, S., McNamara, A. K., Kubo, A., Speziale, S., Miyagi, L., Meng, Y., et al. (2007). Deformation of (Mg,Fe)SiO3 post-perovskite and D″ anisotropy. *Science*, *316*(5832), 1729–1732. https://doi.org/10.1126/science.1140609

Merkel, S., Wenk, H. R., Shu, J., Shen, G., Gillet, P., Mao, H.-k., & Hemley, R. J. (2002). Deformation of polycrystalline MgO at pressures of the lower mantle. *Journal of Geophysical Research*, *107*(B11). ECV 3-1-ECV 3-17. https://doi.org/10.1029/2001JB000920

Miyagi, L., Nishiyama, N., Wang, Y., Kubo, A., West, D. V., Cava, R. J., et al. (2008). Deformation and texture development in CaIrO3 post-perovskite phase up to 6 GPa and 1300 K. *Earth and Planetary Science Letters*, *268*(3), 515–525. https://doi.org/10.1016/j.epsl.2008.02.005

Miyagi, L., & Wenk, H. R. (2016). Texture development and slip systems in bridgmanite and bridgmanite + ferropericlase aggregates. *Physics and Chemistry of Minerals*, *43*(8), 597–613. https://doi.org/10.1007/s00269-016-0820-y

Morgan, W. J. (1971). Convection plumes in the lower mantle. *Nature*, *230*(5288), 42–43. https://doi.org/10.1038/230042a0

Moulik, P., & Ekstrom, G. (2014). An anisotropic shear velocity model of the Earth's mantle using normal modes, body waves, surface waves and long-period waveforms. *Geophysical Journal International*, *199*(3), 1713–1738. https://doi.org/10.1093/gji/ggu356

Mulyukova, E., Steinberger, B., Dabrowski, M., & Sobolev, S. V. (2015). Survival of LLSVPs for billions of years in a vigorously convecting mantle: Replenishment and destruction of chemical anomaly. *Journal of Geophysical Research*, *120*(5), 3824–3847. https://doi.org/10.1002/2014jb011688

Nakagawa, T., & Tackley, P. J. (2008). Lateral variations in CMB heat flux and deep mantle seismic velocity caused by a thermal-chemical-phase boundary layer in 3D spherical convection. *Earth and Planetary Science Letters*, *271*(1–4), 348–358. https://doi.org/10.1016/j.epsl.2008.04.013

Nowacki, A., & Cottaar, S. (2021). Toward imaging flow at the base of the mantle with seismic, mineral physics, and geodynamic constraints. In *Mantle convection and surface expressions* (pp. 329–352). https://doi.org/10.1002/9781119528609.ch13

Nowacki, A., & Wookey, J. (2016). The limits of ray theory when measuring shear wave splitting in the lowermost mantle with ScS waves. *Geophysical Journal International*, *207*(3), 1573–1583. https://doi.org/10.1093/gji/ggw358

Nowacki, A., Wookey, J., & Kendall, J. M. (2010). Deformation of the lowermost mantle from seismic anisotropy. *Nature*, *467*(7319), 1091–1094. https://doi.org/10.1038/nature09507

Nowacki, A., Wookey, J., & Kendall, J. M. (2011). New advances in using seismic anisotropy, mineral physics and geodynamics to understand deformation in the lowermost mantle. *Journal of Geodynamics*, *52*(3), 205–228. https://doi.org/10.1016/j.jog.2011.04.003

Olson, P., Hinnov, L. A., & Driscoll, P. E. (2014). Nonrandom geomagnetic reversal times and geodynamo evolution. *Earth and Planetary Science Letters*, *388*, 9–17. https://doi.org/10.1016/j.epsl.2013.11.038

Pachhai, S., Li, M., Thorne, M. S., Dettmer, J., & Tkalčić, H. (2021). Internal structure of ultralow-velocity zones consistent with origin from a basal magma ocean. *Nature Geoscience*, *15*(1), 79–84. https://doi.org/10.1038/s41561-021-00871-5

Pisconti, A., Creasy, N., Wookey, J., Long, M. D., & Thomas, C. (2023). Mineralogy, fabric and deformation domains in D″ across the southwestern border of the African LLSVP. *Geophysical Journal International*, *232*(1), 705–724. https://doi.org/10.1093/gji/ggac359

Pisconti, A., Thomas, C., & Wookey, J. (2019). Discriminating between causes of D″ anisotropy using reflections and splitting measurements for a single path. *Journal of Geophysical Research*, *124*(5), 4811–4830. https://doi.org/10.1029/2018JB016993

Reali, R., Van Orman, J. A., Pigott, J. S., Jackson, J. M., Boioli, F., Carrez, P., & Cordier, P. (2019). The role of diffusion-driven pure climb creep on the rheology of bridgmanite under lower mantle conditions. *Scientific Reports*, *9*(1), 2053. https://doi.org/10.1038/s41598-018-38449-8

Reiss, M. C., Long, M. D., & Creasy, N. (2019). Lowermost mantle anisotropy beneath Africa from differential SKS-SKKS shear-wave splitting. *Journal of Geophysical Research*, *124*(8), 8540–8564. https://doi.org/10.1029/2018JB017160

Ritsema, J., Deuss, A., van Heijst, H. J., & Woodhouse, J. H. (2011). S40RTS: A degree-40 shear-velocity model for the mantle from new Rayleigh wave dispersion, teleseismic traveltime and normal-mode splitting function measurements. *Geophysical Journal International*, *184*(3), 1223–1236. https://doi.org/10.1111/j.1365-246X.2010.04884.x

Ritsema, J., Lay, T., Garnero, E. J., & Benz, H. (1998). Seismic anisotropy in the lowermost mantle beneath the Pacific. *Geophysical Research Letters*, *25*(8), 1229–1232. https://doi.org/10.1029/98GL00913

Ritsema, J., van Heijst, H. J., & Woodhouse, J. H. (2004). Global transition zone tomography. *Journal of Geophysical Research*, *109*(B2), B02302. https://doi.org/10.1029/2003jb002610

Romanowicz, B., & Wenk, H.-R. (2017). Anisotropy in the deep Earth. *Physics of the Earth and Planetary Interiors*, *269*, 58–90. https://doi.org/10.1016/j.pepi.2017.05.005

Spencer, A. J. M. (1980). *Continuum mechanics*. Courier Corporation.

Steinberger, B., & Calderwood, A. R. (2006). Models of large-scale viscous flow in the Earth's mantle with constraints from mineral physics and surface observations. *Geophysical Journal International*, *167*(3), 1461–1481. https://doi.org/10.1111/j.1365-246X.2006.03131.x

Steinberger, B., & Holme, R. (2008). Mantle flow models with core-mantle boundary constraints and chemical heterogeneities in the lowermost mantle. *Journal of Geophysical Research*, *113*(B5). https://doi.org/10.1029/2007jb005080

Suzuki, Y., Kawai, K., & Geller, R. J. (2021). Imaging paleoslabs and inferring the Clapeyron slope in D″ beneath the northern Pacific based on high-resolution inversion of seismic waveforms for 3-D transversely isotropic structure. *Physics of the Earth and Planetary Interiors*, *321*, 106751. https://doi.org/10.1016/j.pepi.2021.106751

Tackley, P. J. (2011). Living dead slabs in 3-D: The dynamics of compositionally-stratified slabs entering a "slab graveyard" above the core-mantle boundary. *Physics of the Earth and Planetary Interiors*, *188*(3–4), 150–162. https://doi.org/10.1016/j.pepi.2011.04.013

To, A., Romanowicz, B., Capdeville, Y., & Takeuchi, N. (2005). 3D effects of sharp boundaries at the borders of the African and Pacific Superplumes: Observation and modeling. *Earth and Planetary Science Letters*, *233*(1–2), 137–153. https://doi.org/10.1016/j.epsl.2005.01.037

Torsvik, T. H., Burke, K., Steinberger, B., Webb, S. J., & Ashwal, L. D. (2010). Diamonds sampled by plumes from the core-mantle boundary. *Nature*, *466*(7304), 352–355. https://doi.org/10.1038/nature09216

Torsvik, T. H., Steinberger, B., Ashwal, L. D., Doubrovine, P. V., & Trønnes, R. G. (2016). Earth evolution and dynamics—A tribute to Kevin Burke. *Canadian Journal of Earth Sciences*, *53*(11), 1073–1087. https://doi.org/10.1139/cjes-2015-0228

Vanacore, E., & Niu, F. (2011). Characterization of the D″ beneath the Galapagos Islands using SKKS and SKS waveforms. *Earthquake Science*, *24*(1), 87–99. https://doi.org/10.1007/s11589-011-0772-8

Walker, A. M., Dobson, D. P., Wookey, J., Nowacki, A., & Forte, A. M. (2018). The anisotropic signal of topotaxy during phase transitions in D. *Physics of the Earth and Planetary Interiors*, *276*, 159–171. https://doi.org/10.1016/j.pepi.2017.05.013

Walker, A. M., Forte, A. M., Wookey, J., Nowacki, A., & Kendall, J. M. (2011). Elastic anisotropy of D″ predicted from global models of mantle flow. *Geochemistry, Geophysics, Geosystems*, *12*(10), Q10006. https://doi.org/10.1029/2011gc003732

Wang, Y., & Wen, L. (2007). Complex seismic anisotropy at the border of a very low velocity province at the base of the Earth's mantle. *Journal of Geophysical Research*, *112*(B9). https://doi.org/10.1029/2006JB004719

Ward, J., Walker, A. M., Nowacki, A., Panton, J., & Davies, J. H. (2024). The sensitivity of lowermost mantle anisotropy to past mantle convection. *Physics of the Earth and Planetary Interiors*, *356*, 107264. https://doi.org/10.1016/j.pepi.2024.107264

Wenk, H. R., Canova, G., Bréchet, Y., & Flandin, L. (1997). A deformation-based model for recrystallization of anisotropic materials. *Acta Materialia*, *45*(8), 3283–3296. https://doi.org/10.1016/S1359-6454(96)00409-0

Wenk, H.-R., Cottaar, S., Tomé, C. N., McNamara, A., & Romanowicz, B. (2011). Deformation in the lowermost mantle: From polycrystal plasticity to seismic anisotropy. *Earth and Planetary Science Letters*, *306*(1–2), 33–45. https://doi.org/10.1016/j.epsl.2011.03.021

Wolf, J., Creasy, N., Pisconti, A., Long, M. D., & Thomas, C. (2019). An investigation of seismic anisotropy in the lowermost mantle beneath Iceland. *Geophysical Journal International*, *219*(Supplement_1), S152–S166. https://doi.org/10.1093/gji/ggz312

Wolf, J., Li, M., & Long, M. D. (2024). Low-velocity heterogeneities redistributed by subducted material in the deepest mantle beneath North America. *Earth and Planetary Science Letters*, *642*, 118867. https://doi.org/10.1016/j.epsl.2024.118867

Wolf, J., Li, M., Long, M. D., & Garnero, E. (2024). Advances in mapping lowermost mantle convective flow with seismic anisotropy observations. *Reviews of Geophysics*, *62*(2), e2023RG000833. https://doi.org/10.1029/2023RG000833

Wolf, J., & Long, M. D. (2022). Slab-driven flow at the base of the mantle beneath the northeastern Pacific Ocean. *Earth and Planetary Science Letters*, *594*, 117758. https://doi.org/10.1016/j.epsl.2022.117758

Wolf, J., & Long, M. D. (2023). Lowermost mantle structure beneath the central Pacific Ocean: Ultralow velocity zones and seismic anisotropy. *Geochemistry, Geophysics, Geosystems*, *24*(6), e2022GC010853. https://doi.org/10.1029/2022GC010853

Wolf, J., & Long, M. D. (2024). ScS shear-wave splitting in the lowermost mantle: Practical challenges and new global measurements. *Seismica*, *3*(1). https://doi.org/10.26443/seismica.v3i1.1128

Wolf, J., Long, M. D., & Frost, D. A. (2024). Ultralow velocity zone and deep mantle flow beneath the Himalayas linked to subducted slab. *Nature Geoscience*, *17*(4), 302–308. https://doi.org/10.1038/s41561-024-01386-5

Wolf, J., Long, M. D., Li, M., & Garnero, E. (2023). Global compilation of deep mantle anisotropy observations and possible correlation with low velocity provinces. *Geochemistry, Geophysics, Geosystems*, *24*(10), e2023GC011070. https://doi.org/10.1029/2023GC011070

Wookey, J., Kendall, J.-M., & Rümpker, G. (2005). Lowermost mantle anisotropy beneath the north Pacific from differential S—ScS splitting. *Geophysical Journal International*, *161*(3), 829–838. https://doi.org/10.1111/j.1365-246X.2005.02623.x

Wu, X., Lin, J. F., Kaercher, P., Mao, Z., Liu, J., Wenk, H. R., & Prakapenka, V. B. (2017). Seismic anisotropy of the D″ layer induced by (001) deformation of post-perovskite. *Nature Communications*, *8*(1), 14669. https://doi.org/10.1038/ncomms14669

Yamazaki, D., & Karato, S.-I. (2007). Lattice-preferred orientation of lower mantle materials and seismic anisotropy in the D″ layer. In *Post-Perovskite: The last mantle phase transition* (pp. 69–78). https://doi.org/10.1029/174GM07

Yamazaki, D., Yoshino, T., Ohfuji, H., Ando, J.-i., & Yoneda, A. (2006). Origin of seismic anisotropy in the D″ layer inferred from shear deformation experiments on post-perovskite phase. *Earth and Planetary Science Letters*, *252*(3), 372–378. https://doi.org/10.1016/j.epsl.2006.10.004

Yoshida, M. (2008). Core-mantle boundary topography estimated from numerical simulations of instantaneous mantle flow. *Geochemistry, Geophysics, Geosystems*, *9*(7), Q07002. https://doi.org/10.1029/2008gc002008

Yuan, Q., Li, M., Desch, S. J., Ko, B., Deng, H., Garnero, E. J., et al. (2023). Moon-forming impactor as a source of Earth's basal mantle anomalies. *Nature*, *623*(7985), 95–99. https://doi.org/10.1038/s41586-023-06589-1

Yuan, Q., & Li, M. (2022a). Instability of the African large low-shear-wave-velocity province due to its low intrinsic density. *Nature Geoscience*, *15*(4), 334–339. https://doi.org/10.1038/s41561-022-00908-3

Yuan, Q., & Li, M. (2022b). Vastly different heights of LLVPs caused by different strengths of historical slab push. *Geophysical Research Letters*, *49*(17), e2022GL099564. https://doi.org/10.1029/2022gl099564

Zhang, N., Zhong, S., Leng, W., & Li, Z.-X. (2010). A model for the evolution of the Earth's mantle structure since the Early Paleozoic. *Journal of Geophysical Research*, *115*(B6), B06401. https://doi.org/10.1029/2009jb006896

Zhang, N., & Zhong, S. J. (2011). Heat fluxes at the Earth's surface and core-mantle boundary since Pangea formation and their implications for the geomagnetic superchrons. *Earth and Planetary Science Letters*, *306*(3–4), 205–216. https://doi.org/10.1016/j.epsl.2011.04.001

Zhong, S., McNamara, A., Tan, E., Moresi, L., & Gurnis, M. (2008). A benchmark study on mantle convection in a 3-D spherical shell using CitcomS. *Geochemistry, Geophysics, Geosystems*, *9*(10), Q10017. https://doi.org/10.1029/2008gc002048